SANDIA REPORT

SAND2003-3613
Unlimited Release
Printed December, 2003

Equations of State for Hydrogen and Deuterium

Gerald I. Kerley, Consultant

Prepared by
Sandia National Laboratories
Albuquerque, New Mexico 87185 and Livermore, California 94550

Sandia is a multiprogram laboratory operated by Sandia Corporation,
a Lockheed Martin Company, for the United States Department of Energy's
National Nuclear Security Administration under Contract DE-AC04-94AL85000.

Sandia National Laboratories

Issued by Sandia National Laboratories, operated for the United States Department of Energy by Sandia Corporation.

Available to DOE and DOE contractors from
U.S. Department of Energy
Office of Scientific and Technical Information
P.O. Box 62
Oak Ridge, TN 37831

Telephone: (865)576-8401
Facsimile: (865)576-5728
E-Mail: reports@adonis.osti.gov
Online ordering: http://www.doe.gov/bridge

Available to the public from
U.S. Department of Commerce
National Technical Information Service
5285 Port Royal Rd
Springfield, VA 22161

Telephone: (800)553-6847
Facsimile: (703)605-6900
E-Mail: orders@ntis.fedworld.gov
Online order: http://www.ntis.gov/help/ordermethods.asp?loc=7-4-0#online

SAND2003-3613
Unlimited Release
Printed December 1, 2003

Equations of State for Hydrogen and Deuterium

Gerald I. Kerley, Consultant
Kerley Technical Services
P.O. Box 709
Appomattox, VA 24522-0709

Abstract

This report describes the complete revision of a deuterium equation of state (EOS) model published in 1972. It uses the same general approach as the 1972 EOS, i.e., the so-called "chemical model," but incorporates a number of theoretical advances that have taken place during the past thirty years. Three phases are included: a molecular solid, an atomic solid, and a fluid phase consisting of both molecular and atomic species. Ionization and the insulator-metal transition are also included. The most important improvements are in the liquid perturbation theory, the treatment of molecular vibrations and rotations, and the ionization equilibrium and mixture models. In addition, new experimental data and theoretical calculations are used to calibrate certain model parameters, notably the zero-Kelvin isotherms for the molecular and atomic solids, and the quantum corrections to the liquid phase. The report gives a general overview of the model, followed by detailed discussions of the most important theoretical issues and extensive comparisons with the many experimental data that have been obtained during the last thirty years. Questions about the validity of the chemical model are also considered. Implications for modeling the "giant planets" are also discussed.

Acknowledgements

Sandia is a multiprogram laboratory operated by Sandia Corporation, a Lockheed Martin Company, for the United States Department of Energy's National Nuclear Security Administration under Contract DE-AC04-94AL85000. I am grateful to Marcus Knudson and Jim Asay for supporting this work. I especially appreciate the encouragement Marcus has given me during the difficulties of the past year.

Contents

Figures

Symbols and Units

ρ	density [g/cm^3]
V	specific volume, $V = 1/\rho$ [cm^3/g]
T	temperature [K]
P	pressure [GPa]
E	specific internal energy [MJ/kg]
A	Helmholtz free energy [MJ/kg]
S	entropy [$MJ/(kg\text{-}K)$]
K	isothermal bulk modulus, $K = \rho(\partial P/\partial\rho)_T$ [GPa]
W	atomic or molecular weight [*g/mole or kg/kg-mole*]
Z	atomic number [*unitless*]
k	Boltzmann's constant [1.38066×10^{-29} MJ/K]
β	$1/kT$
N_0	Avogadro's number [6.02214×10^{23} $mole^{-1}$ = 6.02214×10^{26} $(kg\text{-}mole)^{-1}$]
R	gas constant [$R = N_0k = 8.31451\times10^{-3}$ $MJ/kg\text{-}mole\text{-}K$]
h	Planck's constant [6.62608×10^{-40} $MJ\text{-}s$]
Γ	Grüneisen parameter [*unitless*]
Θ	Debye or Einstein temperature [K]
C_S	sound velocity [*km/s*]
U_S	shock velocity [*km/s*]
u_P	particle velocity [*km/s*]

1. Introduction

This report discusses new equations of state (EOS) for hydrogen (H_2) and deuterium (D_2). These new EOS were constructed using an updated version of a D_2 EOS model originally developed in 1972 [1]-[3]. The current work employs essentially the same approach, but it incorporates refinements to the theory as well as new experimental data that have become available during the last thirty years.

The old D_2 EOS, described in Refs. [1]-[3], is often called the "Sesame EOS." However, it actually predated the Sesame library by several years and did not use the approximations that were often made in generating EOS tables during those early years.[1] It employed two concepts that later came to be known as the "chemical model" and the "linear mixing approximation."

We will refer to the original model as the "1972 EOS" in this report. It was constructed using a multiphase, multicomponent, chemical equilibrium model that included dissociation, ionization, and the insulator-metal transition. The general approach can be summarized as follows.

- Separate EOS were constructed for the molecular solid, the monatomic solid, the molecular fluid, and the monatomic fluid. They were combined into a single table using the principles of phase transitions and chemical equilibrium.
- The EOS for the molecular solid included contributions from the zero-Kelvin isotherm, lattice vibrations, and internal vibration and rotation.
- The EOS for the monatomic solid included contributions from the zero-Kelvin isotherm, lattice vibrations, and thermal electronic excitation and ionization. The insulator-metal transition was built into the zero-Kelvin and thermal electronic terms.
- The EOS for the molecular and atomic fluids were constructed from a variational theory of liquids called the CRIS model [1].[2] The fluid EOS also included the same vibrational-rotational and thermal electronic terms as in the solid EOS.
- The EOS for the molecular and atomic fluids were combined into a single EOS for the fluid phase using the linear-mixing approximation and the assumption of chemical equilibrium. The model predicted a transition from a molecular fluid to a metallic atomic fluid at high pressures but did not predict phase separation between the two constituents in the fluid phase.

1. The term "Sesame" does not refer to any particular EOS model. It refers to a database of EOS that have been constructed using a variety of models and put into tabular form, primarily for use in hydrocode calculations. The new EOS tables discussed in this report have also been tabulated in the Sesame format and so are also "Sesame EOS."
2. In fact, the CRIS model was originally developed for use in the deuterium EOS, especially the atomic fluid.

Of course, the EOS of hydrogen has continued to be the subject of much experimental and theoretical work during the last thirty years.[1] Experimental techniques can now access much higher pressures—an order of magnitude higher for shock wave methods [4]-[10], *two* orders of magnitude higher for static methods [11][12]. A number of alternative chemical models have also appeared [13]-[17]. There have been many quantum-mechanical calculations for various structures of the molecular and atomic phases [18]-[21]. Improvements in computers and computational methods now allow *ab initio* numerical computation of the EOS surface over a wide range of densities and temperatures [22]-[27]. Almost all of this work has validated the basic concepts and approach used in the 1972 EOS model.

There is one exception that is still an area of controversy. In 1997-98, a group at Lawrence Livermore National Laboratory reported deuterium Hugoniot data at pressures 25-400 GPa, obtained using the Nova laser [28]-[30]. Those experiments gave shock compressions as much as 45% higher than predicted by the 1972 EOS. Later experiments using the Nike laser at the Naval Research Laboratory gave similar results [31][32]. Many papers have since appeared to offer explanations for the discrepancy and models that are in better agreement with the laser data.

However, recent theoretical and experimental research has cast doubt on the validity of the laser results. *Ab initio* numerical calculations do not reproduce the large shock compressions, agreeing much better with the 1972 EOS [22]-[27]. That work strongly suggests that the Nova and Nike laser data are inconsistent with an equilibrium theory of the shock behavior.

Even more important, recent Hugoniot experiments on D_2 contradict the laser results and are in good agreement with both the 1972 EOS and the *ab initio* calculations. Knudson, et al. [6][7], have obtained data at pressures in the range 20-100 GPa, using magnetically-driven flyers generated by the Z-machine at Sandia National Laboratories. The flyer technique generates a steady, flat-topped shock over a longer time interval than was available in the laser experiments; therefore these data are more accurate than the Nova/Nike laser data. Trunin, et al. [9], and Belov, et al. [10], have used spherically-converging shock generators to obtain Hugoniot data for liquid and solid deuterium at pressures near 60 GPa. Their data are consistent with the Sandia flyer data, the 1972 EOS, and the *ab initio* calculations. Recent laser experiments using impedance matching methods, not yet published, are also reputed to be in general agreement with the data in Refs. [6]-[10].

Nellis [33] has also noted that the high compressions reported in the Nova laser experiments are inconsistent with the behavior seen in other diatomic molecules. The more recent experiments [6]-[10], the 1972 EOS, and the *ab initio* calculations

1. Hundreds of publications on this subject have appeared in the last thirty years. We will not try to summarize all of this work. The references given here are the ones most relevant to the present study.

are all reasonably consistent with Hugoniot data for other diatomics. Nellis also discusses possible causes of experimental error in the laser experiments.

We believe it is now clear that the Nova/Nike laser data in Refs. [28]-[32] either contain systematic errors or nonequilibrium effects that have not yet been identified. We will proceed on that assumption in the present work. Arguments in support of this conclusion are discussed in Appendix A.

Since the 1972 model is in fairly good agreement with all of the other data, as well as the *ab initio* calculations, we will also assume that no major conceptual changes are necessary.[1] However, a number of refinements and improvements are needed. The new calculations were made using the PANDA code [34], a more modern EOS program developed and used for modeling many other materials during the intervening years. PANDA includes significant improvements to the liquid model [35]-[38], the mixture model [39][40], and the ionization equilbrium model [41][42]. In addition, more recent experimental and theoretical results can be used to give a better description of the zero-Kelvin isotherms for both the molecular and metallic phases. When all of these changes are included, the new calculations give better agreement with the recent shock wave data and *ab initio* calculations.[2]

The remainder of this report is organized as follows.

- Section 2 discusses the chemical model and addresses questions about its validity at high densities.
- Section 3 gives a broad overview of the theoretical model.
- Section 4 discusses the zero-Kelvin isotherms for the molecular and atomic solids.
- Section 5 discusses the lattice-dynamical terms in the solid EOS.
- Section 6 discusses the fluid perturbation theory (CRIS model) and presents a new model for the quantum corrections.
- Section 7 discusses the treatment of internal molecular vibrations and rotations, with emphasis on anharmonicity and density effects.
- Section 8 discusses the ionization equilibrium model, used for computing the thermal electronic terms in the EOS.
- Section 9 discusses the mixture/chemical equilibrium model and the effects of partial immiscibility between molecules and atoms.
- Section 10 compares the model predictions with experimental data.
- Conclusions and recommendations are given in Section 11.

1. Despite the success of the 1972 EOS in matching the data obtained in the subsequent thirty years, chemical models are still criticized as being inappropriate at high pressures. These criticisms will be addressed in Section 2.
2. Some of this work has already been discussed elsewhere. The improved liquid model was applied to molecular hydrogen and deuterium in Refs. [37] and [38], but a completely new EOS table was not generated at that time. A completely new deuterium table was generated in 1998, for presentation at a meeting in Livermore, CA, but that work was not published. The present work includes many improvements to the 1998 model.

2. The Chemical Model

The present work is based upon the "chemical picture" of matter, in that it assumes the existence of distinguishable chemical species—molecules, atoms, electrons, and ions. A number of recent papers have challenged the validity of this picture, especially at high densities. Proponents of the so-called "physical picture" correctly observe that electrons and nuclei are the only fundamental particles in quantum statistical mechanics. According to this view, *ab initio* numerical methods are necessary for an accurate description of high-density matter.

The harshest critics of the chemical picture insist that high-density matter is best regarded as a "soup" of electrons and nuclei and that "molecules" and "atoms" are artificial, even naive, concepts. Since the present work invokes the chemical picture, these comments must be addressed. Our view can be summarized as follows:

- The "soup" picture is indeed correct at very high densities; in fact, it is the high-density limit of our model.
- Molecular concepts are still useful at the densities typically encountered in the shock regime, including reflected shocks.
- However, chemical models *do* need to account for perturbations that lead to the instability of molecular vibrations at high densities.

It is important to recognize that H_2 and D_2 molecules are not simply geometrical accidents in which two atoms are temporarily trapped by mutual attractive forces. Molecules are the result of covalent bonds, localized electronic states in which electrons with paired spins are shared by two atoms.[1] Because bonds are localized states, the interactions between electrons *within* a bond is much stronger than the interactions among electrons in *different* bonds. As a result, molecules do not automatically dissociate when they come in contact with other atoms and molecules. Dissociation involves an electronic transition, e.g., to an antibonding state.

Experimental data show that hydrogen and deuterium remain molecular solids at pressures up to 200 GPa (at room temperature)—over *ten-fold* compression relative to liquid density. Spectroscopic measurements show that the molecular vibrational frequency is within 10% of that for the gas phase and that the molecules still *rotate* at high densities [11][12]. These observations show that the molecules are true chemical entities, not simply pairing of atoms in the unit cell. At higher pressures, both materials undergo a transition to a new molecular phase, though the vibrational frequency is more strongly perturbed and the molecules appear to be orientationally ordered. The new phase is stable to the highest pressure yet stud-

1. The description of localized electronic states continues to be a difficult problem in theories of dense matter. Theories that give good results for delocalized states are often inaccurate for localized states, and vice versa.

ied, 342 GPa—*13 times liquid density* [43]. Moreover, the transition pressure increases with temperature, showing that higher temperatures favor the more conventional molecular structure.

The solid data prove that density effects, by themselves, do not destabilize molecules at compressions less than ten-fold. By contrast, single shock experiments achieve a maximum compression of about 4.2, while reflected shock experiments have achieved compressions close to 8. Hence, molecular concepts are meaningful and useful throughout the entire range of shock phenomena.

This observation appears to contradict the results of some *ab initio* calculations at high temperatures, which suggest that molecules lose their identity at much lower densities. These calculations fall into two main categories.

- Density Functional Theory-Molecular Dynamics (DFT-MD) [23][24]: This approach employs several approximations. The electron and ion motions are decoupled by an extension of the Born-Oppenheimer (BO) approximation to finite temperatures.[1] The electronic free energy is computed using an approximate density functional that includes gradient corrections. The ion motion is assumed to be classical and is computed using molecular dynamics.
- Path Integral Monte Carlo (PIMC) [25]-[27]: This approach does not make any of the above approximations and is exact in principle. However, it suffers from numerical problems associated with the cancellation of large positive and negative terms that arise in fermion systems. This difficulty requires the use of numerical techniques that reduce its accuracy at low temperatures.

The *ab initio* calculations have played a very valuable role in understanding the hydrogen EOS. However, it should be recognized that these methods are still not exact. Thus far, neither method has given satisfactory agreement with the experimental Hugoniot data at pressures below 20 GPa, where the shock temperature is too low to cause significant molecular dissociation.[2]

Militzer and Ceperley showed that PIMC calculations for hydrogen were in good agreement with the chemical model of Saumon and Chabrier at densities from 9.83×10^{-4} to 0.153 g/cm^3 (twice the liquid density) and temperatures from 5000 to 250,000K [26].[3] These results show that the chemical picture is not necessarily in-

1. The original BO approximation applies only to a single electronic state [44]. The nuclei are held fixed while solving the Schrödinger equation for the electrons; the electronic energy, which depends on the nuclear positions, is then used as the potential for the nuclear motion. In the finite temperature version [45], the nuclei are held fixed while computing the free energy, both a spatial and *thermal* average over all electronic states; the electronic free energy is then used as the potential for the nuclear motion. The accuracy of this approximation apparently has not been studied.
2. We expect that these difficulties can and will be overcome eventually.
3. The Saumon-Chabrier model also agrees well with our 1972 EOS in this regime [14].

consistent with the physical picture, even if the latter is more fundamental. Militzer and Ceperley did observe small deviations at the highest densities, which they attributed to inaccuracies in the chemical picture. (We will show that our model gives good agreement with their calculations in Sec. 10.)

Galli, et al., used the DFT-MD method to study deuterium at four- and six-fold compressions and at temperatures from 5000 to 10,000K [24]. They found that molecules have short lifetimes at high densities—only one vibrational period in some cases. Their interpretation of these results was that such "molecules" are little more than brief encounters between individual atoms, not real chemical entities as at lower densities. But there are two reasons for disputing this conclusion.

- Short molecular lifetimes do not necessarily contradict the chemical picture. At equilibrium, the rates of formation and dissociation of molecules must be equal. Therefore, the equilibrium EOS is determined by the total *number* of molecules present at a given instant, *not the lifetimes* of individual molecules. Molecules can make a significant contribution to the partition function even if they are short-lived.[1]
- The DFT-MD method is likely to underestimate the stability of molecules at high densities. The approximate density functional and the expansion of the electronic states as plane waves should not be expected to describe localized molecular bonding accurately [46]. The classical description of the molecular vibrations and rotations may also be a source of error. Finally, extension of the BO approximation to thermal averages may not be accurate when the electron and ion degrees of freedom are strongly coupled, as they are in molecules. (See Sec. 7.4 for further discussions.)

However, it can be shown that ultra-high densities *do* destabilize molecular vibrations. In fact, this effect was included in our 1972 EOS model [2]. The argument, discussed further in Sec. 7, is as follows. Because of anharmonicity in the intramolecular potential, only a finite number of rotational and vibrational states can exist; the highest allowed levels are determined by the dissociation energy. The effective dissociation energy decreases with increasing density, giving fewer allowed vibrational states. According to the model used in the present work, the dissociation energy drops to zero at 23 times liquid density. At higher densities, no vibrational states are available, and molecules are not allowed. The level cutoff also affects the contribution of molecules at high temperatures, favoring dissociation. Chemical models that do not account for vibrational destabilization will not give the correct limit—the electron-ion "soup"—at high densities. But chemical models *can* be expected to give a realistic description of matter, even at ultra-high densities, if the effect of vibrational destabilization is included.

1. An analogous situation occurs in the ionization equilibrium of high-Z elements. Autoionizing states (multiple electron excitations having energies above the normal ionization limit) have short lifetimes but make large contributions to the partition function.

3. Model Overview

As already noted, the EOS model used here is essentially a refinement of that used in our 1972 EOS. It includes three phases—a molecular solid, an atomic solid, and a fluid phase that allows both molecular and atomic chemical species. Separate EOS tables were constructed for the molecular solid, the molecular fluid, the atomic solid, and the atomic fluid. A single EOS table for the fluid phase, accounting for dissociation, was computed using the PANDA mixture/chemical equilibrium model. The multiphase EOS table was then assembled from the EOS tables for the fluid phase and the two solid phases, using the PANDA phase transition model. The EOS for the atomic fluid includes electronic excitation and ionization, so that the model is valid at arbitrarily high temperatures and densities.

The primary emphasis in this work is given to the properties of the fluid phase, the phase most important to dynamic experiments and applications. The molecular solid is represented by a single phase; we have not included the solid phases that have been discovered in recent diamond anvil experiments at very high pressures, at and below room temperature [11].[1] Neither have we attempted to model anharmonic effects on the solid behavior, requiring only reasonable agreement with the solid data and the melting curves of the two isotopes.

In this section, we will give a broad overview of the model and how its parts fit together. Detailed discussions about different aspects of the theory and model parameters are given in Sections 4-9. Section 9 also discusses the importance of chemical species other than molecules and atoms in the fluid phase. The model predictions are discussed and compared with experiment in Sec. 10.

3.1 Solid Phases

The thermodynamic functions for the molecular and atomic solids were expressed as sums of terms that were assumed to be separable and additive:

$$P(\rho, T) = P_c(\rho) + P_l(\rho, T) + P_{vr}(\rho, T) + P_e(\rho, T), \quad (1)$$

$$E(\rho, T) = E_c(\rho) + E_l(\rho, T) + E_{vr}(\rho, T) + E_e(\rho, T) - \Delta E_0, \quad (2)$$

$$A(\rho, T) = E_c(\rho) + A_l(\rho, T) + A_{vr}(\rho, T) + A_e(\rho, T) - \Delta E_0. \quad (3)$$

The subscript c denotes the zero-Kelvin curve, which is discussed in Sec. 4. The subscript l denotes contributions from lattice vibrations, discussed in Sec. 5. The

1. These phases could be included in our EOS, but we are not aware of any demand for this extension of our model. Therefore, we have chosen to devote our time to issues of greatest relevance to the dynamic experiments and applications.

subscript *vr* denotes contributions from molecular vibration and rotation, which were included only for the molecular phase; these terms are discussed in Sec. 7. The subscript *e* denotes contributions from thermal electronic excitations, which were included only for the atomic phase; these terms are discussed in Sec. 8. In order to give a consistent energy zero for all phases, the constants ΔE_0 were chosen to give zero enthalpy for the molecular gas at room temperature (298K) and atmospheric pressure (1.0135×10^{-4} GPa).

3.2 Molecular and Atomic Fluid Phases

Our model for the fluid phases differs from that for the solid phases in an important way: *contributions from the zero-Kelvin isotherm and the thermal motion of the molecules are not treated as separable and additive.* In fluids, the molecules have sufficient thermal energy to escape the local potential wells around the equilibrium solid lattice positions, giving rise to a random structure. Therefore, fluid theories require a different approach than solid theories. Our calculations employ liquid perturbation theory—a version called the CRIS model [36][38]—that has been shown to give very good results for all kinds of fluids.

Using this theory, the thermodynamic functions for the molecular and atomic fluids were given by the following expressions.

$$P(\rho, T) = P_\phi(\rho, T) + P_{vr}(\rho, T) + P_e(\rho, T) \tag{4}$$

$$E(\rho, T) = E_\phi(\rho, T) + E_{vr}(\rho, T) + E_e(\rho, T) - \Delta E_0 \tag{5}$$

$$A(\rho, T) = A_\phi(\rho, T) + A_{vr}(\rho, T) + A_e(\rho, T) - \Delta E_0 . \tag{6}$$

Here the subscript ϕ denotes the contributions from the intermolecular forces and the thermal motions of the molecular centers of mass, which is computed from the CRIS model, which is discussed in Sec. 6. The subscript *vr* denotes the contribution from the molecular vibration and rotation (molecular fluid only), and *e* denotes the contribution from thermal electronic excitations (atomic fluid only); these two terms are the same as for the solid phases and are discussed in Secs. 7 and 8, respectively. The constants ΔE_0 were chosen to give zero enthalpy for the molecular gas at room temperature and atmospheric pressure, just as for the solid phases.

3.3 The Fluid Mixture

The fluid model discussed above, Eqs. (4)-(6), describes the EOS for a single chemical component, either molecules or atoms. The PANDA mixture model was used to construct the EOS for the multicomponent fluid. Separate EOS tables were first constructed for each chemical constituent in the mixture. An EOS for the mixture was then constructed using the ideal mixing approximation, the chemical

composition at each density and temperature being determined from the principle of chemical equilibrium. The mixture model is discussed in Sec. 9.

3.4 The Multiphase EOS

The PANDA phase transition model was used to construct the final multiphase EOS. Separate EOS tables were first constructed for the molecular solid, the atomic solid, and the multicomponent fluid. PANDA computes the phase boundaries by locating the pressure-temperature points at which the Gibbs free energies of two or more phases are equal, then constructs the final multiphase table. (See Sec. 11 of the PANDA manual for further details.)

3.5 The Final EOS Tables

The hydrogen EOS was tabulated on a grid of 95 density points, from 0.0 to 50 g/cm^3, and 80 temperature points, from 5 to 1.0x10^8 K. The density-temperature points were selected to resolve structure in the EOS, including the vapor-liquid coexistence region. Maxwell constructions were included at temperatures from the boiling point, 20.39K, to the calculated critical point, 31.71K, leaving a tension region at low temperatures. The material number is 5250.

The deuterium EOS was tabulated on a similar density-temperature grid, but the density range is from 0.0 to 100 g/cm^3. Maxwell constructions were included at temperatures from the boiling point, 23.10K, to the calculated critical point, 38.80K. The material number is 5260.

4. Zero-Kelvin Isotherms

In our 1972 model, the zero-Kelvin isotherm for the molecular phase was constructed from the static data of Stewart [47] and the calculations of Liberman [48], while that for the atomic phase was constructed from the calculations of Neece, et al. [49] and Bardeen [50]. In this work, we have used more current information to construct new isotherms for the two phases—the molecular isotherm was constructed from the static data of Anderson and Swenson [51] and Loubeyre, et al. [52], while the atomic isotherm was constructed from the calculations of Ceperley, et al. [19][21]. The changes to the isotherms result in significant differences between the new model and the 1972 EOS.

Two points should be clarified before beginning the discussion. First, the zero-Kelvin isotherms needed for our models must include *only* the contributions from the intermolecular forces. The contributions from the molecular motions, including zero-point vibrations, are taken into account elsewhere in both the solid and liquid models. Hence, corrections for the zero-point energy and pressure must be made to the experimental data used in constructing the isotherms.[1]

Second, we assume that the intermolecular forces for hydrogen and deuterium are identical for all practical purposes. It follows that the isotherms for both isotopes are identical when expressed in terms of mole units instead of mass units. Hence the same parameters are used for both isotopes, except for scaling by the ratio of the molecular weights. (Specifically, the density of deuterium at a given pressure is 1.998 that for hydrogen, while the specific internal energy (per unit mass) is 0.5004 that for hydrogen.)

Of course, molecular weight scaling is exact only for the zero-Kelvin isotherms. It is *not* exact after the molecular motions are taken into account [53].

4.1 Molecular Phase

The zero-Kelvin isotherm for the molecular phase was constructed in two parts. At low pressures, we used the so-called EXP-N option in PANDA (Sec. 3.4 of Ref. [34]). The pressure and energy are given by

$$P_c(\rho) = [\rho_0 E_B \nu/(1-3\nu/\alpha)]\{\eta^{2/3}\exp([\alpha(1-\eta^{-1/3})]-\eta^{\nu+1})\}, \quad (7)$$

$$E_c(\rho) = [E_B/(1-3\nu/\alpha)]\{(3\nu/\alpha)\exp[\alpha(1-\eta^{-1/3})]-\eta^{\nu}\}, \quad (8)$$

1. Note that the zero-point corrections were also included in our 1972 model.

where $\eta = \rho/\rho_0$, ρ_0 and E_B are the density and binding energy at zero pressure, and α and ν are constants. The exponential terms in Eqs. (7) and (8) represent the contributions from repulsive forces, which are controlled by the parameter α; this constant is related to the bulk modulus at zero pressure by

$$K_0 = \rho_0 E_B \nu(\alpha/3 - 1/3 - \nu)/(1 - 3\nu/\alpha). \quad (9)$$

The terms involving η^ν represent the contributions from attractive forces. At large separations, the attractive terms can be expressed in a multipole expansion in inverse powers of the intermolecular distance [54]. For non-polar molecules, the leading term in this expansion varies as the 6th power, corresponding to ν = 2.0. However, Silvera and Goldman [54] have noted that 8th, 9th, and 10th power terms are also important for the hydrogen isotopes, suggesting that a larger value of ν would be appropriate.

In this work, we chose the parameters ρ_0, E_B, and K_0 by fitting the static compression data for solid H_2 and D_2 [51][52] (after correcting for the zero-point energy). We found that ν = 2.5 gave better results for the liquid and vaporization properties than ν = 2.0. Our parameters for the two isotopes are as follows.

H_2 $\rho_0 = 0.1335$ g/cm^3 $E_B = 1.30$ MJ/kg $K_0 = 1.15$ GPa $\nu = 2.5$

D_2 $\rho_0 = 0.2668$ g/cm^3 $E_B = 0.6505$ MJ/kg $K_0 = 1.15$ GPa $\nu = 2.5$

The EXP-N formula does not give satisfactory results at high pressures because it does not have the correct asymptotic form as $\rho \to \infty$. (The exponential term approaches a constant value with increasing density, while the magnitude of the attractive term continues to increase.) Equation (7) gives good agreement with the static high-pressure data for solid H_2 and D_2 up to about 14 GPa, where it begins to underestimate the pressure.

In order to remedy the high-density problem, the PANDA code offers a formula known as the "TFD match" (Sec. 3.6 of Ref. [34]). At densities greater than a user-specified value ρ_m, the energy is given by

$$E_c(\rho) = [E_T(\rho) - E_T(\rho_m)](1 + b_1/\rho + b_2/\rho^{4/3} + b_3/\rho^{5/3}) + b_0, \quad (10)$$

where $E_T(\rho)$ is a fit to the energy obtained from Thomas-Fermi-Dirac (TFD) theory, and the constants b_0 - b_3 are determined by requiring continuity of the energy, the pressure, and the first two density derivatives of the pressure.

Hence ρ_m is the only input variable for this expression. The high-pressure portion of the cold curves for H_2 and D_2 are quite sensitive to this parameter. The values used in this work were $\rho_m = 0.285$ g/cm^3 for H_2 and $\rho_m = 0.57$ g/cm^3 for D_2.

Figure 1 compares our model fits with experimental static compression data for solid H_2. The crosses are from Anderson and Swenson at 4.2K [51], while the circles are from Loubeyre, et al., at 300K [52]. In order to compare with the experimental data, the lattice-dynamical terms (Sec. 5) were also included in computing the model curves, shown by solid and dashed lines, respectively.

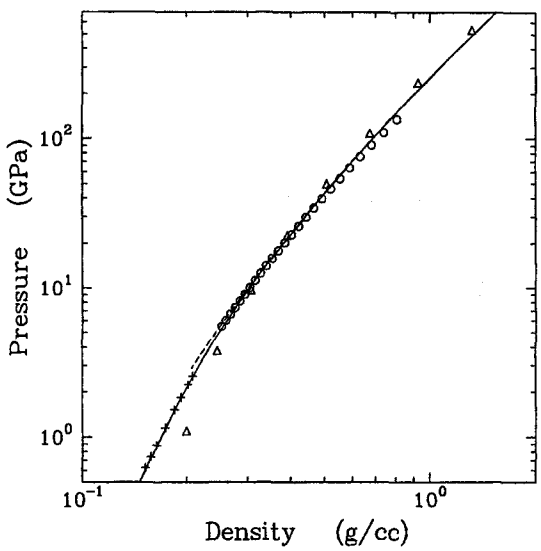

Fig. 1. Static compression curves for molecular hydrogen. Experiment: crosses—4.2K [51], circles—300K [52]. Model calculations are shown by solid and dashed curves. Triangles are calculations of Liberman [48].

The calculations of Liberman [48] (which do not include the lattice-dynamical terms) are shown by triangles in Fig. 1. His work, first reported in 1971, has received little attention in the literature. His isotherm is somewhat stiffer than the most recent data, but the agreement is impressive in view of the fact that it preceded the experiments by 25 years. Liberman's calculations were used to construct the zero-Kelvin curve in our 1972 EOS model.

The results for D_2 are virtually identical to those for H_2, except for a factor of two in density.

Our model parameters give a slightly stiffer static compression curve than that reported by Loubeyre, et al. [52]—roughly 4% lower in density at the highest pressure. This result represents a compromise between matching the static and shock-wave data. Better agreement with the static data can be obtained using a larger value of ρ_m. However, a softer cold curve gives unsatisfactory agreement with the Hugoniot data.

Because the shock-wave data correspond to the fluid phase, some stiffening of the solid cold curve can be justified on theoretical grounds. Loubeyre, et al., note that the c/a ratio for solid hcp hydrogen deviates from the ideal value, 1.633, decreasing with increasing pressure. They attribute this effect to orientational ordering; the density would be expected to decrease if the molecules were rotating freely. When the c-axis is expanded to give the ideal value, the density decreases by about 3% at the highest pressure. There is also a small negative zero-point pressure term that arises from the decrease in vibron frequency with density at high pressures. When both of these corrections are included, the resulting cold curve is quite close to that used in our model.

Unfortunately, the above argument does not completely resolve the discrepancy between the static and shock-wave data within the framework of our model. Perfect agreement with shock data would require an even stiffer cold curve, one close to the calculations of Liberman (as used in the 1972 EOS). But we cannot justify such a stiff cold curve in light of the static data. However, the parameters used here still give acceptable agreement with the Hugoniot data, as shown in Sec. 10.

4.2 Atomic Phase

Because there are no experimental data for the atomic solid phases, it is necessary to rely on theoretical calculations of the cold curves. Many calculations have been performed during the last thirty years, but there is a startling lack of agreement among them. Uncertainties in the exchange-correlation potential and treatment of the coupling between the electron and proton motions contribute to the theoretical difficulties [55][56].

Min, et al. [18], and Barbee, et al. [20], computed the cold curve for the sc, bcc, and fcc phases of atomic hydrogen using the local density approximation (LDA) for the exchange-correlation potential. Min, et al., obtained zero-pressure densities 0.54-0.56 g/cm^3 and binding energies 99-114 MJ/kg, depending on lattice structure (when zero-point motion is not included). Barbee, et al., obtained similar densities but much lower binding energies, 79-95 MJ/kg.

Ceperley and Alder (CA) [19] used the quantum Monte Carlo (QMC) method to compute the cold curves for the same three phases. They performed calculations in which the electron and proton motions were completely coupled (the dynamic lattice) and also where the proton motion was suppressed (the static lattice). Their results for the static lattice were significantly different from those obtained with the LDA model—a zero-pressure density of 0.6 g/cm^3 and binding energy of 69 MJ/kg.

Because the QMC method is nominally exact, CA asserted that their calculations were more accurate than the LDA predictions. In practice, however, the accuracy of their method is determined by several factors—including the use of a trial wavefunction to fix the position of the fermion nodes, and the limitation to a relatively small number of particles per unit cell. Careful procedures were used to extrapolate the finite-number results to an infinite number of particles, but the corrections were very large.

Subsquently, Natoli, et al. [21], repeated the QMC calculations using a much better trial wavefunction to fix the nodes. Unfortunately, they only presented results at single density, 1.2 g/cm^3, well above the zero-pressure point, focusing primarily on differences between various lattice structures. For the bcc phase, the energy was roughly 10 MJ/kg lower than that reported by CA at the same density. A shift

of -10 MJ/kg in the energy would bring the binding energy close to the results of Barbee, et al. The changes in the trial function had less effect on the pressure and the difference between the static and dynamic curves.

It is clear that more theoretical and calculational work is needed to determine the cold curves for the atomic solids with confidence. In the meantime, we have used the CA calculations, adjusted as follows: CA give an analytic formula for the energy vs. density for the dynamic lattice, with parameters fit to the numerical calculations (Eq. 11 of Ref. [19]). We modified two of the three fit parameters to obtain better agreement with the energy and pressure reported by Natoli, et al., for the bcc lattice at 1.2 g/cm^3. (The new values were d_1, d_2, d_3 = -0.2078, 0.0437, -0.0301, compared with -0.2166, 0.0566, -0.0301 given by CA.) The energy and pressure for the static lattice were computed by subtracting a fit to the CA zero-point term, using the formula given in Sec. 6. With these changes, the cold curve comes much closer to the LDA results.

The results were fit to the same expression as for the molecular solids—the EXP-N formula, Eqs. (7) and (8), with the high-density TFD match, Eq. (10). Our parameters for the two isotopes are as follows.

H_1 $\rho_0 = 0.5662$ g/cm^3 $E_B = 82.45$ MJ/kg $K_0 = 95$ GPa $\nu = 1.4$ $\rho_m = 1.0$ g/cm^3

D_1 $\rho_0 = 1.131$ g/cm^3 $E_B = 41.26$ MJ/kg $K_0 = 95$ GPa $\nu = 1.4$ $\rho_m = 2.0$ g/cm^3

Figure 2 shows the cold curves for solid atomic hydrogen. Circles are the CA calculations with the adjustment discussed above; the lower curve is for the static lattice (no zero-point motion), and the upper curve is for the dynamic lattice (with zero-point motion). The solid curves are the corresponding model fits. The LDA calculations of Min, et al. [18], are shown by diamonds. Squares are the TFD results.

The cold curves for solid atomic deuterium are similar except for a factor of 2 in the density. In addition, the offset between the static and dynamic curves is a factor of $\sqrt{2}$ less than for hydrogen.

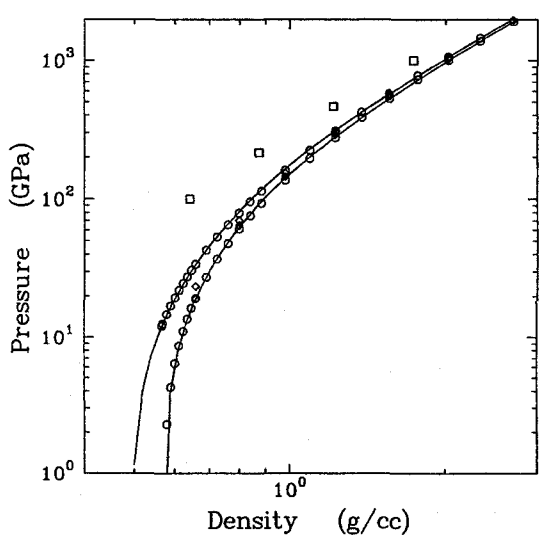

Fig. 2. Static compression curves for atomic hydrogen. Circles are calculations of Ceperley and Alder [19], adjusted as discussed in text. Diamonds are calculations of Min, et al. [18]. Model calculations are shown by solid curves. Squares are TFD calculations.

5. Lattice-Dynamical Terms

In our 1972 EOS, the lattice-vibrational terms were computed from the free-volume cell model for the molecular phase and the Debye model for the atomic phase. The cell model gives a good description of anharmonic effects but does not treat quantum effects, such as the zero-point energy. In the present work, the Debye model was used for both phases; it treats the quantum effects but gives a less accurate description of anharmonic effects.

The equations for the Debye model are well-known and will be omitted here. (They are given in Sec. 4.2 of the PANDA manual [34]; we used the option that excludes lattice vibrations with unrealistically large amplitudes.) The following formulas (option IGRN=4 in PANDA) were used to treat the density-dependence of the Debye temperature Θ and Grüneisen function Γ.

$$\Theta(\rho) = \Theta_{ref}(\rho/\rho_{ref})^{1/2} \exp\{[\Gamma_{ref}-\Gamma(\rho)]/\tau\}, \tag{11}$$

$$\Gamma(\rho) = (\Gamma_{ref}-1/2)(\rho_{ref}/\rho)^{\tau} + 1/2, \tag{12}$$

where Θ_{ref}, Γ_{ref}, ρ_{ref}, and τ are constants.

5.1 Molecular Solid

The parameters Θ_{ref} and Γ_{ref} for H_2 were taken from the measurements of Krause and Swenson [57], specifically the value on the melting line at 52K, which corresponds to ρ_{ref} = 0.1245 g/cm^3. The value of Θ_{ref} for D_2 was obtained by scaling that of H_2 according to the square root of the molecular weight. The value of τ was chosen to give the best possible fit to the melting data of Diatshenko, et al. [58]. The resulting values were:

H_2	ρ_{ref} = 0.1245 g/cm^3	Θ_{ref} = 255 K	Γ_{ref} = 1.82	τ = 1.38
D_2	ρ_{ref} = 0.2488 g/cm^3	Θ_{ref} = 180 K	Γ_{ref} = 1.82	τ = 1.70

Note that different values of τ were required for the two isotopes, in order to obtain the best agreement with the melting data. The need for this inconsistency is most likely due to the effects of anharmonic behavior on the lattice vibrations.

5.2 Atomic Solid

As for the cold curve, there is considerable disparity among the various theoretical predictions of the lattice-dynamical motion in atomic hydrogen. Once again, the QMC method, used by Ceperley and Alder [19], gives a nominally exact treat-

ment of the coupling between the electron and proton motions (at 0K). The Debye temperature can be computed from the difference between their static and dynamic curves. Moreover, the numerical refinements introduced by Natoli, et al. [21], gave the same offset between the static and dynamic curves for the bcc lattice at the one density studied.[1]

In the present work, we found that Eqs. (11) and (12) give a satisfactory fit to the CA results for the zero-point proton motion. The resulting values were:

H_1 $\rho_{ref} = 0.5662$ g/cm^3 $\Theta_{ref} = 2168$ K $\Gamma_{ref} = 1.063$ $\tau = 1.5$

D_1 $\rho_{ref} = 1.131$ g/cm^3 $\Theta_{ref} = 1534$ K $\Gamma_{ref} = 1.063$ $\tau = 1.5$

As an aside, we note that these values for Θ_{ref} and Γ_{ref} agree with the Slater and free-volume formulas [34] to within 20%.

1. Natoli, et al., found significant differences in the zero-point motion for the various lattice structures. The phase transitions in solid atomic hydrogen is an interesting issue, but we do not address it in this work, because we are focusing primarily on the fluid region.

6. The Liquid Model

The EOS for both the molecular and atomic fluids employ a version of liquid perturbation theory called the CRIS model, originally developed for use in the 1972 model of deuterium. The original version used a first-order approximation for the free energy [1]. The model was later improved to include corrections beyond first order, which are especially important for metallic fluids, and quantum corrections, which are important for the hydrogen isotopes [36][38]. This improved CRIS model has been shown to give good results for a wide variety of liquids—molecular [38][40][59]-[61], metallic [62]-[66], non-metallic [42], and ionic [67].

The model is amply discussed elsewhere [34]-[36][38], and only a few points will be reviewed here. However, the treatment of the quantum corrections, which is new to the present study, will be discussed in detail.

6.1 The Variation-Perturbation Method

The thermodynamic properties of a fluid are determined by the potential energy ϕ of a molecule in the field of neighboring molecules. The free energy A_ϕ can be written in terms of this function by using a perturbation expansion about the properties of an idealized hard-sphere fluid,

$$A_\phi(\rho, T) = A_0(\rho, T, \sigma) + N_0\langle\phi\rangle_0 + \Delta A_{qm} + \Delta A_{ho}, \tag{13}$$

where N_0 is Avogadro's number. Here A_0 is the free energy for a fluid of hard spheres, the first-order term $N_0\langle\phi\rangle_0$ is an average of ϕ over all configurations of the hard sphere fluid, and ΔA_{qm} is the quantum correction (see below). These three terms comprise the first-order estimate of the free energy, which is a rigorous upper bound to the exact value. ΔA_{ho}, by definition, includes all higher-order terms in the expansion and is negative for all values of σ. In the CRIS model, the hard-sphere diameter σ is defined by maximizing the first-order free energy (which is equivalent to minimizing $|\Delta A_{ho}|$) with respect to σ at each density and temperature. This variational approach selects the hard-sphere system having a structure that is closest to that of the real fluid. The corrections ΔA_{ho} are then computed from approximate expressions. The pressure and energy are computed from the standard thermodynamic relations.

The high-order corrections ΔA_{ho}, which were not included in our 1972 EOS, are significant for the hydrogen isotopes and are partly responsible for the fact that our new EOS predicts higher shock compressions.

The function ϕ depends upon the intermolecular forces and the configuration of neighbors around a particular molecule. The current state of the art is not suffi-

ciently advanced to allow an accurate determination of this function from either experiment or theory. In the CRIS model, this function is estimated from the zero-Kelvin energy of the solid phase by

$$N_0\phi \approx (\rho/\rho_s)E_c(\rho_s), \tag{14}$$

where ρ is the actual density of the fluid, and ρ_s is the solid density having the same nearest neighbor distance as that of a particular fluid configuration. (The zero-Kelvin isotherms for the molecular and atomic phases are discussed in Sec. 4.) Equation (14) is strictly applicable only for additive forces and must be modified at high densities. This modification is discussed in Sec. 6.4.

Finally, $\langle\phi\rangle_0$ is computed by averaging the function ϕ over all nearest neighbor distances, using a weighting function derived from the radial distribution function for hard-spheres.

6.2 Comments on the CRIS Model

The CRIS model differs from other liquid theories in that the intermolecular forces are expressed in terms of a zero-Kelvin isotherm for the solid instead of a pair potential. It is important to recognize that this approximation does *not* require the assumption that the liquid structure is "solid-like."[1] Indeed, Rosenfeld [68][69] has shown that, for the case of pair-wise additive forces, the CRIS model is mathematically equivalent to perturbation theories that employ pair potentials. But a formulation based upon the solid isotherm is much more useful than one based on pair potentials when non-additive forces are present. This approach gives good results for metallic and ionic fluids as well as molecular fluids.

The fluid model plays a very important role in understanding and calculating the EOS of the hydrogen isotopes. Approaches using "effective" pair potentials can and do give reasonable results in the molecular regime, but they break down when dissociation becomes important, because the atomic fluid becomes metallic at high densities and the interatomic forces cannot be expressed by such potentials. Advanced quantum-mechanical theories should eventually allow a more rigorous treatment of the intermolecular forces, but they still have limitations as discussed in Sec. 2.

In Sec. 3, we commented that solid-like models do not give satisfactory results in the liquid regime, i. e., that contributions from the zero-Kelvin isotherm and the thermal motion of the molecules cannot be treated as separable and additive. Despite this fact, it is still a common practice among EOS modelers to use equations

1. Our early reports on the CRIS model [1]-[3] did invoke the physical picture of a liquid as a "mixture of solid-like clusters." This concept did not prove to be helpful and was later abandoned. The theory was put on a more rigorous basis in subsequent papers [35][36][38].

like (1)-(3) to describe the fluid regime. It is often assumed that such models will give reasonable results when the lattice vibrational terms are modified to give the ideal gas formula at high temperatures and/or low densities. These "solid-gas" interpolation models have been applied to the hydrogen isotopes [15]-[17], but they do not give satisfactory agreement with the experimental data. Although the CRIS model also makes use of the solid isotherm, it gives results quite different from the simple interpolation models.

In applying the CRIS model to a given material, it may be necessary to decide which of several solid structures gives the cold curve most appropriate for modeling the liquid. However, this issue seldom causes a problem in practice. We have found that the close-packed structures (fcc, hcp, and bcc) generally give the best results, and the differences between these structures are usually small. For atomic hydrogen and deuterium, for which several structures have been postulated, the differences are smaller than the uncertainties in any particular structure.

6.3 Quantum Corrections

In previous work [34][38], we approximated the quantum term ΔA_{qm} in Eq. (13) by the quantum correction for hard spheres given by Singh and Sinha [70]. We have reexamined this term in the present study and found that approach to be unsatisfactory. The magnitude of the quantum corrections for the hydrogen isotopes can be estimated from data for liquid hydrogen and deuterium reported by Mills, et al. [71]-[74], as discussed below. We found that the expansion given in Ref. [70] gave reasonable results at low densities but underestimated the quantum corrections at higher densities. Higher-order formulas for hard spheres [75][76] were also tried but found to overestimate the quantum corrections. Including quantum corrections to the hard-sphere radial distribution function (in calculating $\langle\phi\rangle_0$) might improve the results but would substantially complicate the theory.

Rosenfeld [68][69] has shown that the quantum corrections in the CRIS model can be related to the Einstein oscillator frequency for the solid. We have used a modified form of his approach in this work. Rosenfeld considered the case in which the forces between molecules are given by an additive pair potential $u(r)$. The quantum corrections can be computed to first-order by adding a quantum term to the potential,

$$u(r) \rightarrow u(r) + u_{qm}(r) = u(r) + (\lambda^2/24\pi)\nabla^2 u(r), \tag{15}$$

where $\lambda = (h^2/2\pi WkT)^{1/2}$ is the thermal wavelength. The solid isotherm is a sum of the potential between a given molecule and all its neighbors in the lattice.

$$E_c(\rho_s) = (1/2)\sum n_k u(r_k), \tag{16}$$

where n_k and r_k are the number and distance of the neighbors in the k-th shell, respectively. When the quantum term is added to the potential, Eq. (14) becomes

$$\phi \rightarrow \phi + \phi_{qm} = (\rho/\rho_s)[E_c(\rho_s) + (h^2/96\pi^2 WkT)\sum n_k(\nabla^2 u)_k]. \quad (17)$$

so that

$$\Delta A_{qm} = (N_0/W)\langle\phi_{qm}\rangle_0. \quad (18)$$

Rosenfeld observed that ϕ_{qm} can be expressed in terms of the Einstein oscillator frequency, as follows. Let ξ_c be the energy of a molecule displaced by a distance r from its equilibrium lattice position. Expanding the potential in a Taylor series about the displacement, one obtains

$$\xi_c(r;\rho_s) = \frac{1}{2}\sum n_k u(r_k) + \frac{1}{4}\sum n_k(\nabla^2 u)_k\, r^2 + \ldots = E_c(\rho_s) + \frac{3}{2}W\nu_E^2 r^2 + \ldots, \quad (19)$$

where ν_E is the Einstein frequency of oscillation for a molecule in the lattice, its neighbors being held fixed. Comparing Eqs. (17) and (19), we find that

$$\phi_{qm} = (\rho/\rho_s)(h^2\nu_E^2/16\pi^2 kT) = (\rho/\rho_s)(k\Theta_E^2/4T), \quad (20)$$

where $\Theta_E = h\nu_E/2\pi k$ is the Einstein temperature.

The Einstein temperature can also be estimated from density derivatives of the zero-Kelvin isotherm, eliminating the need for a pair potential. In order to obtain a suitable expression, we calculated the lattice sum as a function of density using an exponential-6 (Buckingham) potential with parameters typical for hydrogen, computing Θ_E exactly. A satisfactory fit to the exact calculations was obtained with the formula

$$\Theta_E \approx 106(W/\rho_s)^{1/6}\sqrt{(K_c - 1.645P_c)/W}\ \text{Kelvin}.^1 \quad (21)$$

The density dependence in Eq. (21) is identical to that for the so-called "free-volume" formula for the Grüneisen function [34][77], except that the pressure is multiplied by the factor 1.645 instead of 4/3.

Equation (20) must be modified to give reasonable behavior at low temperatures. The following expression was found to give satisfactory results for hydrogen.

$$\phi_{qm} = (\rho/\rho_s)[0.25kTx_E^2/(1 + x_E/6)], \quad (22)$$

1. Θ_E is set to zero at low densities, where $K_c - 1.645P_c < 0$. This regime has little effect because the quantum corrections are small at low densities.

where $x_E = q_E\Theta_E/T$ and q_E is an adjustable parameter. Using Eq. (22), ϕ_{qm} goes to the zero-point energy of an Einstein oscillator at zero temperature [34].

Equations (18), (21), and (22) define our model for the quantum corrections as implemented in the PANDA code. To test this model, we made Monte Carlo calculations of the first-order quantum corrections for an exponential-6 pair potential by making appropriate modifications to the PANDA Monte Carlo option (Section 15.4 of Ref. [34]). The Einstein oscillator formula was in good agreement with those calculations.

The quantum corrections for the hydrogen isotopes were also estimated from the experimental compression data [71]-[74] for liquid hydrogen and deuterium, by assuming the corrections to be inversely proportional to molecular weight, as implied by Eqs. (17) and (18). Neither the Einstein oscillator formula *nor* the Monte Carlo calculations gave satisfactory agreement with these estimates. It was necessary to set $q_E = 1.90$ for H_2 and $q_E = 1.85$ for D_2 in order to obtain agreement. (Slightly different values were used for the two isotopes in order to get the best agreement with the liquid densities.) This fact suggests that quantum corrections beyond first-order are important for the hydrogen isotopes. However, the formulas presented here give a satisfactory fit to the experimental data when the empirical adjustment is made.

6.4 Adjustments to Model

The CRIS model requires only the solid zero-Kelvin isotherm to generate the thermodynamic properties throughout the entire fluid region; all other parameters are defaulted. However, the PANDA code offers three adjustable parameters that can be used to "fine tune" the fluid EOS. We would naturally prefer to avoid the use of these "knobs" as much as possible. However, they do offer a way to make small adjustments that improve agreement with experimental data.

The first adjustable parameter, the multiplier q_E on the quantum-mechanical term, has already been mentioned. For the sake of consistency, the values obtained by matching static compression data for the molecular fluids were also used for the atomic fluids.

In working with the EOS of metallic fluids, we have generally found two other adjustable parameters to be useful. The first, and most important, is a multiplier (denoted w_X in PANDA) that is applied to the high-order free energy term, ΔA_{ho}, which is especially large for metals. In previous work on nine metallic fluids (Be, C, Ti, Fe, Cu, Ni, W, Au, Pb), we found that multipliers on the order of 2-3 were typically needed to match the liquid entropy at the melting point. In the present work, we have used a multiplier $w_X = 2$ in the EOS for the atomic fluids. (No multiplier was used for the molecular fluids.)

In Sec. 6.2, we noted that Eq. (14) is approximate and must be corrected for the effects of non-additive forces. The equation used in PANDA is [34]

$$N_0\phi = \{[1-f(\rho_s)]\rho/\rho_s + f(\rho_s)(\rho/\rho_s)^{2/3}\}[E_c(\rho_s) - \varepsilon_X], \tag{23}$$

where

$$f(\rho_s) = \exp(-b_X/\rho_s^{1/3}),\ b_X = (0.23 + 0.6544Z^{2/3})(W/Z)^{1/3}. \tag{24}$$

Here W is the atomic weight and Z is the atomic number, so that $b_X = 0.887$ for hydrogen and $b_X = 1.12$ for deuterium. ε_X is an adjustable parameter.

Equations (23) and (24) account for the effects of non-additive forces that occur when the electrons become delocalized at high densities [2][34]. When the model is applied to metals, it is generally found that the parameter ε_X must be set to 3-5% of the total binding energy of the solid in order to match the energy of the liquid at the melting point. Hence this parameter evidently corrects for the delocalization effects that are present in liquid metals. In the present work, we have taken ε_X to be 4% of the solid binding energy.

The parameters w_X and ε_X do not have a drastic effect on the model predictions. We have included them primarily because they give slightly better agreement with the shock-wave data in the regime where dissociation is important.

7. Molecular Vibrations and Rotations

Our model for the vibrational-rotational terms includes the effects of anharmonicity, centrifugal distortion, vibration-rotation coupling, and destabilization of vibrational motion at high densities. These effects were also included in our 1972 model. In this section, we take a fresh look at these issues and approach the problem from a different point of view. We will show that the effects of anharmonicity and vibrational destabilization are important for hydrogen and deuterium.

We consider the vibrational-rotational terms for the isolated molecule first, then extend the model to consider the effects of density. We also discuss the effects of anharmonicity and vibrational destabilization on the Hugoniot of deuterium.

7.1 Isolated Molecule

The vibration-rotation contribution to the free energy is given by

$$A_{vr} = -(RT/W)\ln Q_{vr}, \tag{25}$$

where Q_{vr} is the partition function for a diatomic molecule,

$$Q_{vr} = \frac{1}{\sigma}\sum_{n,j}(2j+1)\exp[-\beta(\varepsilon_{nj}-\varepsilon_{00})]. \tag{26}$$

Here ε_{nJ} is the energy of a state with vibrational quantum number n and rotational quantum number j. (The zero-point energy ε_{00} is subtracted off because it is assumed to be included in the zero-Kelvin curve.) σ is the symmetry number ($\sigma = 1$ for heteronuclear molecules, $\sigma = 2$ for homonuclear molecules). The sum is taken over all allowed quantum numbers as discussed below. The corresponding contribution to the internal energy is

$$E_{vr} = -T^2\left[\frac{\partial}{\partial T}\left(\frac{A_{vr}}{T}\right)\right]_\rho = \frac{N_0}{W\sigma Q_{vr}}\sum_{n,j}(2j+1)(\varepsilon_{nj}-\varepsilon_{00})\exp[-\beta(\varepsilon_{nj}-\varepsilon_{00})]. \tag{27}$$

The vibrational and rotational energy levels are independent of density for an isolated molecule, so there is no contribution to the pressure.

The Morse function is a fairly good representation of the intramolecular potential for a diatomic molecule. It is given by

$$\upsilon(r) = D_0\{1-\exp[-s(r/r_e-1)]\}^2, \tag{28}$$

where D_0 is the dissociation energy and r_e is the equilibrium nuclear distance of the molecule. A good approximation to the energy levels is

$$\varepsilon_{nj} = \omega_e(n+\tfrac{1}{2}) + B_e j(j+1) - \omega_e x_e (n+\tfrac{1}{2})^2 - d_e j^2(j+1)^2 - \alpha_e(n+\tfrac{1}{2})j(j+1) \qquad (29)$$

The first two terms describe the energy levels of a harmonic oscillator and rigid rotator. The last three terms are corrections due to anharmonicity, centrifugal distortion, and vibration-rotation coupling, respectively. The parameters x_e, d_e, α_e, and s can be expressed in terms of ω_e, B_e, and D_0, as follows.[1]

$$x_e = \frac{\omega_e}{4D_0}, \quad d_e = \frac{4B_e^3}{\omega_e^2}, \quad \alpha_e = 3B_e\left(\sqrt{\frac{B_e}{D_0}} - \frac{2B_e}{\omega_e}\right), \quad s = \frac{\omega_e}{2\sqrt{B_e D_0}}. \qquad (30)$$

The quantum numbers n and j are summed over all bound levels, $\varepsilon_{nj} \le D_0$. We also restrict j to values for which $(\partial\varepsilon_{nj}/\partial j)_n \ge 0$, to ensure the correct behavior of the energy levels. The following parameters were used in this work [78]:

H_2 $\omega_e = 4404.6\ \text{cm}^{-1}$ $B_e = 60.890\ \text{cm}^{-1}$ $D_0 = 55100\ \text{K}$ $r_e = 0.7414\ \text{Å}$ $\sigma = 2$

D_2 $\omega_e = 3116.3\ \text{cm}^{-1}$ $B_e = 30.453\ \text{cm}^{-1}$ $D_0 = 55100\ \text{K}$ $r_e = 0.7415\ \text{Å}$ $\sigma = 2$

Figure 3 shows the vibration-rotation energy of an isolated deuterium molecule as a function of temperature. The solid line was computed by an exact sum over all levels, using Eqs. (26)-(30).[2] Comparison with the rigid rotator-harmonic oscillator (RRHO) approximation (dotted line) shows that the correction terms in Eq. (29) are very important. At high temperatures, the RRHO approximation gives the equipartition result ($E_{vr} \to 2RT/W$ for a diatomic molecule). By contrast, the energy for the exact sum approaches a constant value at high temperature because all levels are fully populated and no more energy can be added to the molecule. At temperatures below 10,000K, the exact sum gives a higher

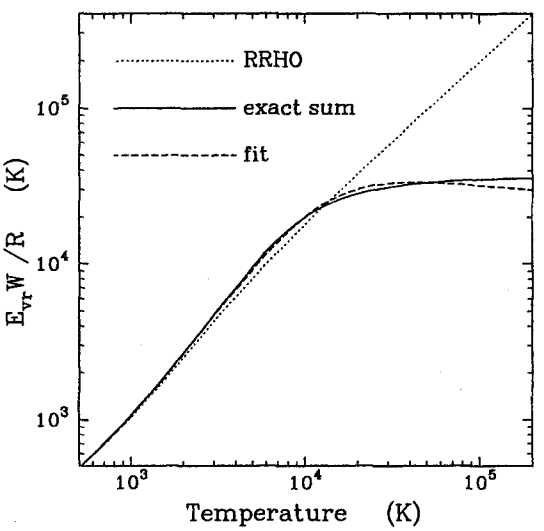

Fig. 3. Vibration-rotation energy of a D_2 molecule as a function of temperature. Curves are defined in the text.

1. For simplicity, we will assume that ω_e, B_e, and D_0 have units of kT in the following equations. In PANDA, ω_e and B_e are entered in wavenumbers (cm^{-1}). (Multiply by 1.43877 to convert from wavenumbers to degrees Kelvin.)

energy than RRHO, due to softening of the vibrational frequency by anharmonicity. We will show below that the corrections to RRHO have a significant effect on the Hugoniot of deuterium.

It is important to recognize that the equipartition principle does not apply in this case, *not even for the rotational degrees of freedom.* When the equipartition principle is applied to the *rigid* rotator, each rotational degree of freedom is found to contribute *kT/2* to the energy of each molecule. But this result is obtained only when all rotational levels are included in the summation. The correct quantum-mechanical analysis of the problem shows that the high-energy rotational levels lead to unstable vibrational states and so must be excluded from the partition function. The contributions from these excluded states correspond to dissociated molecules and are included in the thermodynamic functions for the atomic fluid.

7.2 Analytic Fit

The dashed line in Fig. 3 was computed from an analytic expression obtained by modifying the RRHO formula, as follows. The free energy is given by

$$A_{vr} \approx (RT/W)\ln Q_{rot} + (RT/W)\ln Q_{vib}. \tag{31}$$

The rotational partition function Q_{rot} is given by the standard PANDA approximation for the rigid rotator (Sec. 6.2 of Ref. [34]), modified to include a cutoff at the molecular dissociation energy D_0,

$$Q_{rot} = (1 + x^2 + x^3)^{1/3}, x = [1 - \exp(-\beta D_0)]/\sigma\beta B_e. \tag{32}$$

The vibrational partition function Q_{vib} is given by the harmonic oscillator formula (Sec. 6.3 of Ref. [34]), modified to include both a cutoff at the dissociation energy and temperature-dependence in the vibrational states. The result is

$$Q_{vib} = [1 - \exp(-\beta D_T)]/[1 - \exp(-\beta\omega_T)], \tag{33}$$

where

$$D_T = D_0/(1 + C_T/\beta), \omega_T = \omega_e/(1 + C_T/\beta), \tag{34}$$

and C_T is a constant, given by

2. Note that the *sum* is computed exactly, but the energy level formula, Eq. (29), is approximate. For comparison, we also made calculations using the more elaborate formula given in the JANAF tables [78]. The JANAF formula gives nearly identical results at temperatures up to 10,000K but predicts a higher plateau value at high temperatures. The differences between our model and JANAF are negligible for the purposes of this study.

$$C_T = (x_e + d_e D_0^2/\omega_e B_e^2 + \alpha_e D_0/\omega_e B_e)/2D_0. \quad (35)$$

Equations (34) and (35) account for the effects of anharmonicity, centrifugal distortion, and vibration-rotation coupling. The corresponding contribution to the internal energy can also be computed analytically, from the temperature derivative of the free energy, as in Eq. (27). (We omit the energy equations in the interest of brevity.) This fit was found to give reasonable agreement with the exact sum for H_2, D_2, and several other diatomic molecules.

7.3 Effects of Density

High densities can affect the vibrational and rotational motion of molecules in several ways—hindering the rotational motion, perturbing the vibrational frequency, and destabilizing the vibrational motion by dissociation.

Spectroscopic measurements on solid H_2 and D_2 show that the molecules still rotate or librate in phase I at pressures up to 200 GPa (at room temperature) [11][12]. Measurements of the c/a ratio in the hcp structure suggest that hindering of the rotational motion occurs at the highest pressures [52]. A higher degree of orientational ordering is believed to exist in phase III, which appears above 200 GPa (ten-fold compression) at room temperature [11]. However, the effects of hindering and orientational ordering decrease with increasing temperature, and we do not expect them to be important in the liquid regime. Therefore, we have ignored them in this work.

Spectroscopic measurements on the solids also show that the vibrational frequencies in phase I are perturbed by the forces of neighboring molecules [11]. The vibrational frequency first increases with increasing pressure, reaches a maximum, then decreases at higher pressures. However, the shifts in vibrational frequency are rather small, only about 10% over the entire range studied. While this behavior is interesting and has provoked considerable discussion, these vibrational shifts are too small to have a significant effect on the thermal contributions. (There is a small effect on the cold curve, as mentioned in Sec. 5.2.) More drastic effects on the vibrational motion appear in phase III, but that does not occur until the compression exceeds ten-fold. Therefore, we have ignored perturbations on the vibrational frequency in this work.[1]

The third effect, vibrational destabilization, arises from the decrease in dissociation energy of the molecule by the forces of adjacent molecules. This effect can be estimated in the following way. Let d_{WS} be the diameter of the Wigner-Seitz sphere containing one molecule. A molecule cannot extend outside its own sphere

1. Our 1972 EOS included a treatment of perturbations on the vibrational motion by surrounding molecules. We have decided to abandon that part of the model, rather than revise it to match the more recent spectroscopic data.

without experiencing strong forces from the atoms in adjacent molecules. Let r be the separation between atoms in a molecule. When

$$r + r_e \approx d_{WS} = (6W/\pi N_0 \rho)^{1/3}, \tag{36}$$

the distance between atoms in different molecules is comparable to the equilibrium internuclear distance in a molecule. We use Eq. (36) as the condition for dissociation at high densities. Using the Morse potential, Eq. (28), the corresponding dissociation energy is

$$D(\rho) = D_0\{1 - \exp[-2s\xi(\rho)]\}^2, \xi(\rho) = (\rho_{max}/\rho)^{1/3} - 1, \tag{37}$$

where $\rho_{max} = 3W/4\pi N_0 r_e^3$ is the density at which *all* vibrational levels of a molecule become unstable.

Application of this condition to H_2 and D_2 predicts that molecules will become completely unstable to vibrational motion at 23 times liquid density and a pressure of 1200 GPa for the molecular solids. The destabilization density is about 20% higher than the density at which the molecular solid undergoes a phase transition to the metallic solid.

The effect of density on the vibrational terms is included by replacing the constant D_0 with the function $D(\rho)$ in Eqs. (32) and (34), the other equations in Sec. 7.2 being unchanged. (The density-dependent dissociation energy is not used in the anharmonicity corrections, Eq. (35), because the *shape* of the potential is assumed to be unchanged by vibrational destabilization.)

When the density modifications are included, the vibration-rotation terms make a contribution to the pressure, which is computed from

$$P_{vr} = \rho^2(\partial A_{vr}/\partial\rho)_T. \tag{38}$$

(The specific equations are omitted here in the interest of brevity.)

7.4 Effect on Hugoniot Predictions

Figure 4 shows Hugoniot calculations for molecular deuterium using three different models of the vibration-rotation term. (The effects of dissociation are not included here because we are concerned only with the molecular part of the EOS at this point. Hence the experimental data are not shown either. The effects of dissociation are discussed in Sec. 9, and the full model is compared with experimental data in Sec. 10.)

The dotted curve was computed using the rigid rotator-harmonic oscillator approximation. RRHO predicts the Hugoniot density to increase monotonically with pressure, eventually reaching an asymptote at the expected value, $8\rho_0$.

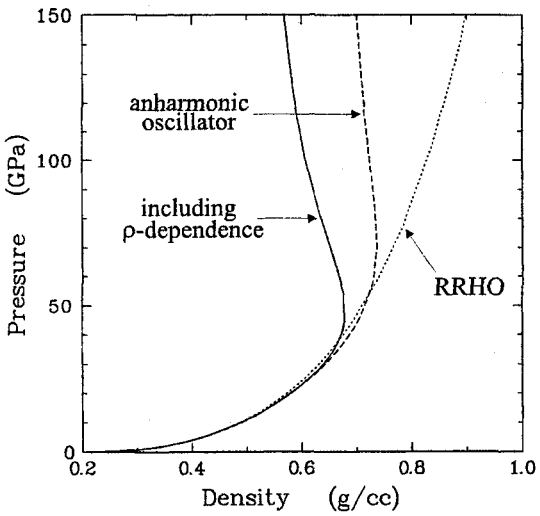

Fig. 4. Sensitivity of D_2 Hugoniot to vibration-rotation model. These calculations do not include dissociation. See text for discussion of curves.

The dashed curve in Fig. 4 was computed including the temperature-dependent terms (Sec. 7.2), which account for the anharmonicity effects. The results are the same as RRHO at low pressures. At pressures in the range 15-50 GPa, the densities are slightly higher than RRHO, because of the additional energy that can be put into the internal degrees of freedom. But the energy cutoff leads to lower densities than RRHO at pressures above 50 GPa. The density reaches a maximum at 70 GPa, then decreases with increasing pressure. The asymptotic value is $4\rho_0$—the correct result for a molecule with no internal degrees of freedom.

The solid curve was computed including the density-dependent destabilization correction (Sec. 7.3) in addition to the temperature-dependent terms. Because the destabilization correction gives a lower cutoff energy, it gives even lower Hugoniot densities at high temperatures. The maximum density is reached at 50 GPa, and the asymptotic value is about $3.3\rho_0$. (The correct asymptotic value, $4\rho_0$, is obtained when dissociation is included, as shown in Sec. 9.)

The effects of anharmonicity and density on molecular stability explain some, but not necessarily all, of the observations of Galli, et al. [24]. High temperatures favor occupation of the vibrational levels closest to the dissociation energy. Because those states have the largest amplitudes of vibration, they are most strongly affected by surrounding molecules and so have shorter lifetimes as the density increases. Our model predicts that effects of density and temperature on the vibration-rotation terms are significant in the regime of their simulations (0.67 and 1.0 g/cm^3, 5000-10,000K). But, as noted in Sec. 2, the approximations made in the DFT-MD method could also lead to spurious results and need to be investigated more carefully before definite conclusions are reached.

8. Ionization Equilibrium Model

The contributions from thermal electronic excitation and ionization to the EOS, subscripted *e* in Eqs. (1)-(6), were computed using the PANDA ionization equilibrium (IEQ) model. This model employs a more fundamental and self-consistent treatment of continuum lowering, pressure ionization, and other problems than the approach used in our 1972 EOS. The IEQ model is also applicable to high-Z elements but simplifies considerably when applied to the hydrogen isotopes.

The IEQ model is discussed in Sec. 9 of the PANDA manual [34]. The version used here includes improvements that are discussed in a recent report on the carbon EOS [42]. We will give an outline of the model here but will not go into all of the details.

8.1 Background

Computation of the thermal electronic terms involves two problems—calculation of the electronic energy levels of the system, and thermal averaging over all levels. The theory of many-electron systems is still not completely solved, and drastic approximations must be made to obtain tractable computational models. Existing models fall into two main types, neither of which gives completely satisfactory results over the entire range of interest.

- Models that use an explicit sum over all electronic configurations of the system normally give the best results at low densities. These models assign the correct statistical weights and perform the thermal averaging correctly, but they make drastic approximations in calculating the energy levels, especially the effects of density. The Saha model [79] is a well-known example of this type.
- At high densities, accurate calculations of the energy levels are needed for best results. However, models capable of such accuracy typically use an average configuration to assign statistical weights and compute electron screening. This approach can give significant errors, particularly when localized states are involved [41][80].[1] The INFERNO model of Liberman [81] is an example of this type.

It is important to distinguish between the terms *average atom* and *average configuration.* In an average atom model, each atom is assigned an identical volumetric region, e.g., a Wigner-Seitz cell or ion sphere. Charge neutrality is imposed upon

1. We note in passing that *ab initio* numerical methods (Sec. 2) do not solve all of these problems. In particular, the DFT-MD method is an average configuration model in that statistical approximations are used to compute the screening and the thermodynamic functions. The PIMC method, while exact in principle, employs similar approximations to eliminate the fermion node problem.

each cell, and the influence of surrounding atoms is approximated by the boundary conditions and the potential outside the cell.

Average configuration models make the additional approximation that the electron screening of the nucleus is the same for all electronic configurations, as discussed above. This approach is not exact, even for an "average" atom; the screening should depend upon the electronic configuration for each state.

8.2 Average Atom Model

The PANDA IEQ model uses the average atom approximation, in that the properties of the system are computed by considering the electronic structure of a single atom. However, the model explicitly sums over all electronic configurations instead of considering a single average configuration. The version of the model used here also includes corrections for thermal fluctuations in charge and volume.

The electronic contribution to the Helmholtz free energy is given by

$$A_e = -(RT/W)\ln q_e, \tag{39}$$

where q_e, the electronic partition function for an average atom, is a sum over all Z+1 states of ionization,

$$q_e = \sum_{z=0}^{Z} q_z \exp[-\beta(\delta_z + u_z + z a_{fz})]. \tag{40}$$

Here a_{fz} is the free energy (per electron) for an electron gas in which there are z free electrons per ion; this quantity is computed from an analytic fit to the homogeneous electron gas that includes the effects of Fermi-Dirac statistics [2]. q_z is the partition function for an ion of charge z, and u_z is the energy of the ion in its ground state configuration. δ_z is a correction to the average atom model, which is discussed below.

The ion partitition function is a sum over all bound-state configurations,

$$q_z = \sum_n g_z(n) \exp[-\beta \varepsilon_z(n)], \tag{41}$$

where $g_z(n)$ and $\varepsilon_z(n)$ are the statistical weights and energy levels of the ion, and the index n is taken over all allowed occupation numbers of the one-electron orbitals. These quantities, along with the ground state energies u_z, are calculated from a scaling model, using a table of orbital radii and energies for the ground state configuration of the isolated atom [82], along with corrections for continuum lowering, as discussed below.

The internal energy E_e and pressure P_e are computed from the temperature and density derivatives of the free energy, using the standard relations. The average ionization state is given by

$$\langle z \rangle = \frac{1}{q_e} \sum_{z=0}^{Z} z q_z \exp[-\beta(\delta_z + u_z + z a_{fz})] . \tag{42}$$

These equations simplify considerably for hydrogen, which has only one electron and two states of ionization. We obtain

$$q_e = q_0 \exp(-\beta\delta_0) + q_1 \exp[-\beta(\delta_1 + I + a_{f1})] , \tag{43}$$

$$\langle z \rangle = (q_1/q_e) \exp[-\beta(\delta_1 + I + a_{f1})] . \tag{44}$$

Here q_0 is a sum over the well-known bound states of the hydrogen atom, $q_1 = 1$ is the partition function for a bare nucleus, and I is the ionization energy of the hydrogen atom.

Equation (44) applies only to the atomic component of the mixture. To allow for the presence of molecules when computing the ionization state, the value of $\langle z \rangle$ must be corrected, using the molar composition obtained from the mixture model.

8.3 Continuum Lowering

At low densities, the Coulomb interactions between the ions and the free electrons can be neglected. However, these interactions become significant at high densities, lowering the energy of the free electron continuum relative to the bound electron levels. Continuum lowering causes the effective ionization energy for the bound electrons to decrease with increasing density. Each bound level has some density at which the ionization energy drops to zero; at higher densities, that level ceases to exist as a bound state and becomes a part of the continuum.

The transition of a level from a bound to free is known as *pressure ionization.* The *insulator-metal transition* occurs when all of the valence-electron levels for the ground state are pressure-ionized. At densities below the transition, the atoms have localized bound states and the material is an insulator (at low temperatures); at densities above the transition, only free-electron states exist and the material is metallic.

The IEQ model computes continuum lowering corrections to the energy levels and statistical weights from the interaction energy between the free electrons, assuming a uniform density within the ion sphere, and the potential of the nucleus as screened by the bound electrons. The resulting equations have been found to

give good agreement with the insulator-metal transition density predicted by the INFERNO code [42].

The equations are particularly simple for the hydrogen isotopes, for which there are no screening effects. The following result is obtained for the ionization energy.

$$I = I_0 - 24.485/r_s \text{ eV}, \tag{45}$$

where I_0 = 13.6025 eV is the ionization of an isolated hydrogen atom, and r_s is the ion-sphere radius in units of the Bohr radius. This relation is also used to cut off the energy levels in computing the atomic partition function q_0. For hydrogen, the insulator-metal transition occurs at r_s = 1.8 or 2.18 cc/g-atom, about 5.5 times liquid density. *Hence all of the principal Hugoniot data for hydrogen and deuterium fall below the insulator-metal transition density.*

Of course, bound states do not simply "disappear" when they cross into the continuum. In principle, the free electron contribution should be corrected to account for nearly bound states, or "resonances." However, we have not yet found a satisfactory way to include these corrections in the IEQ model. As a result, the model predicts discontinuities whenever bound levels are pressure-ionized. Fortunately, these discontinuities do not cause any serious problems for hydrogen and deuterium after the thermal broadening corrections (Sec. 8.5) have been applied.

8.4 Charge Fluctuations

One of the approximations in the average atom model is that charge neutrality holds within an ion sphere. In Ref. [41], we showed that there are fluctuations in the charge within an ion sphere and derived expressions for the correction terms, δ_z, that are valid in the low-density limit. Satisfactory results can be obtained by taking $\delta_z \approx 0$ for $z>1$. (See Ref. [41] for the explicit formulas for δ_0 and δ_1.)

We have not yet found a rigorous theory of charge fluctuations at high densities. However, the fluctuation terms are expected to become less important as the density increases, because of increased attraction between "holes" and "electrons." In order to account for this effect, the low-density values are modified as follows.

$$\delta_z \rightarrow \delta_z \exp(-\kappa\rho/W), \tag{46}$$

where κ is an input parameter, typically on the order of 15 (g-atom/cm^3). This expression was motivated by a model of electrical conductivity data in the vicinity of the insulator-metal transition [83]. A preliminary comparison with the experimental data indicates that it captures the essential features of the physics.

8.5 Thermal Broadening

Another approximation in the average atom model is that all ion spheres are equal in size. In a real material, thermal motions can lead to fluctuations in the sizes of the ion spheres. The current version of PANDA includes a correction for this effect. This correction is discussed in Ref. [42]. We will give only the result here.

Consider a configuration of N atoms in which the ion spheres have volumes $v_1, v_2, \ldots, v_N$ that fluctuate about the average volume $\bar{v}$,

$$\bar{v} = N^{-1} \sum_{i=1}^{N} v_i. \tag{47}$$

We want to average the thermodynamic functions over fluctuations in the ion sphere volume. The dependence of the ion sphere energy on volume is approximated by a second-order Taylor expansion about $\bar{v}$, and the thermal average is then defined using the Boltzmann distribution. After making some simplifying approximations, the following expression for the thermal average of the electronic entropy is obtained.

$$\langle S \rangle \approx \int S(v) \exp[-X_B(v/\bar{v}-1)^2/T]dv / \int \exp[-X_B(v/\bar{v}-1)^2/T]dv, \tag{48}$$

where $X_B = WC_S^2/2R = 60WC_S^2$ (Kelvin), and C_S is the sound speed. In practice, the principal effect of this thermal averaging is to smooth discontinuities that arise when bound levels are cut off due to pressure ionization. The smoothing effect is particularly important in the vicinity of the insulator-metal transition, where the ground state of the atom is pressure-ionized.

In the present version of the model, X_B is taken to be a constant and is treated as an input parameter. Smaller values of X_B give more smoothing. Using the ambient sound speed for the atomic solid, a nominal value for hydrogen is 1.0×10^4 K. However, a smaller value is appropriate in the insulator-metal transition region, where the sound speed is smaller.

8.6 Application to Hydrogen

In the present work, the orbital data used in the atomic scaling model were taken from Ref. [82], except that slight modifications to the orbital binding energies were needed to match the energy levels of the hydrogen atom. The IEQ tables were generated using XB=1.0×10^{-3}K, chosen to give an acceptable amount of smoothing, and $\kappa = 15$. The entropy was tabulated at 54 densities, $1.0\times10^{-10} \le \rho \le 1.0\times10^{3}$ g/cc, and at 36 temperatures, $0 \le T \le 1.16\times10^{8} K$, for both isotopes, the T=0 points being obtained by extrapolation. The entropy tables

were used to compute the thermal electronic contributions to the solid and fluid EOS using the numerical scheme discussed in Sec. 8 of the PANDA manual [34].

The thermal electronic contributions to the entropy and pressure of deuterium are shown in Fig. 5. The curves show isotherms from 1000 to 1.0×10^7K, equally spaced in the logarithm. The most striking feature of the plots is the insulator-metal transition that occurs near a density of 0.9 g/cm^3. At low densities, the 1s valence electron is a localized and insulating state, and the ground state has a statistical weight of 2 corresponding to the two spin orientations. Hence the entropy approaches the value $(R/W)\ln 2 = 0.00286$ MJ/kg/K as $T \rightarrow 0$ at low densities. At high densities, the 1s electrons are pressure-ionized, becoming delocalized, metallic states. The entropy approaches zero as $T \rightarrow 0$ at high densities. This insulator-metal transition results in the dramatic drop in entropy near 0.9 g/cm^3. It also has a significant effect on the pressure—the pressure increases with density below the transition, then drops after the transition is completed.

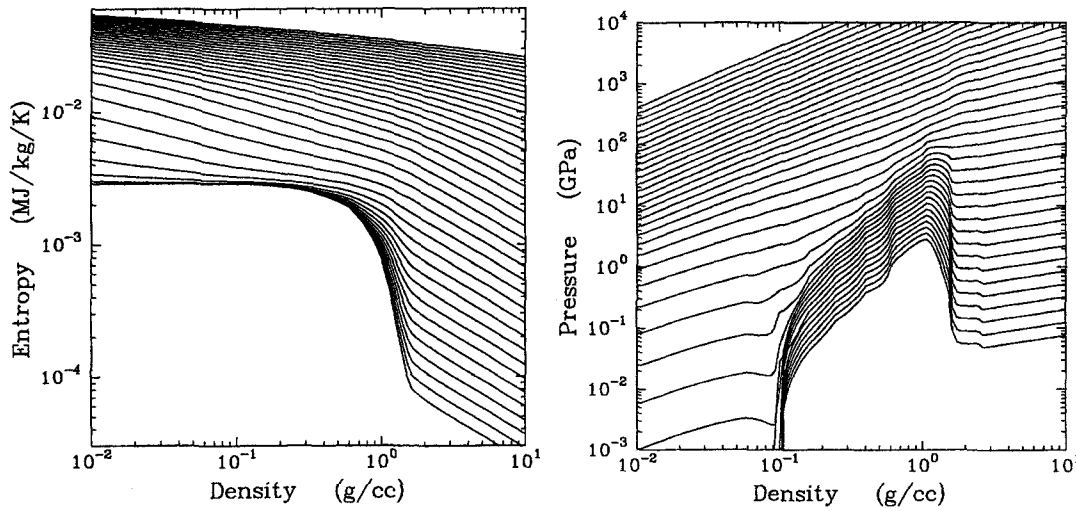

Fig. 5. Thermal electronic contributions to entropy and pressure for atomic deuterium. Curves, calculated from the PANDA IEQ model, show 39 isotherms from 1000 to 1.0×10^7K, equally spaced in the logarithm.

We emphasize that the large jump in entropy at the insulator-metal transition, and the corresponding structure in the pressure, are *not* due to the simplified scheme used to cut off the bound state levels in the IEQ model. The behavior seen in Fig. 5 is observed in all elements, not just hydrogen [42][62]-[66]. Calculations using the INFERNO code also predict this behavior, even though INFERNO treats the bound-free transition in a continuous fashion, using the theory of resonances

[81].[1] This behavior is a characteristic signature of the insulator-metal transition, much as the "van der Waals loop" is characteristic of the vapor-liquid transition.

Like the van der Waals loop, the structure in the thermal electronic pressure has the potential to generate a mechanical instability, leading to a first-order "plasma phase transition" (PPT). In fact, our theoretical models do predict such a PPT for some metallic elements [62][64]-[66]. For atomic H and D, however, there is no instability in the pressure when all terms in the EOS are included. Furthermore, the insulator-metal transition only affects the EOS for the atomic component of the mixture and is obscured by the presence of the molecular component at low temperatures. Therefore, our model does not predict any PPT for the hydrogen isotopes. This result is in agreement with all experimental data available at the present time.

1. However, INFERNO gives the wrong statistical weight for the bound levels, a consequence of the average configuration approximation.

9. Mixture Model

Our 1972 EOS employed a mixture model that has subsequently come to be known as the "linear mixing approximation." The present work uses the PANDA mixture/chemical equilibrium model, which is more accurate. The main improvement is that the PANDA model requires all mixture components to have equal pressures as well as equal temperatures. In the 1972 EOS, the molecular and atomic components were assigned the same density instead of the same pressure.

9.1 Background

While much progress has been made in mixture theory during the past thirty years, there are important problems that have not yet been solved. There is no rigorous mixture theory that can be applied to the present problem. The principal stumbling block comes in dealing with the intermolecular interactions between unlike chemical species. Some mixture theories account for these unlike interactions explicitly, but they apply only to pair-wise additive potentials, an approximation that we want to avoid in this work. Furthermore, these terms are very difficult to determine. They cannot be measured directly, and current quantum-mechanical methods do not offer the necessary accuracy.

PANDA employs the ideal mixing approximation, which only requires EOS for the individual components. The formation of an ideal mixture (also called an ideal solution) can be regarded as a two-step process. First form a heterogenous mixture in which all components have equal pressures and temperatures. Second, allow the components to mix homogeneously, at constant temperature and pressure. In ideal mixing, the second step involves no change in volume or energy, while the entropy change corresponds to complete randomness. The complicated problem of treating unlike interactions is replaced by the simple one of pressure equilibration.

Despite its simplicity, ideal mixing has been found to give good agreement with precise Monte Carlo calculations of mixtures, using hard sphere, soft sphere, and exponential-6 potentials [39][40]. Results were equally good at low and high densities. Perhaps the success of the model is due to the fact that pressure equilibration gives a reasonably accurate treatment of the repulsive forces, i.e., effects of excluded volume, which play the principal role in determining the fluid structure. The equal-density approximation gives less accurate results for the test cases.

One serious flaw in the ideal mixing approximation is that it provides no mechanism for phase separation between components that are immiscible. The PANDA version offers an option for treating immiscible components. It also provides for situations in which the pressure is not a monotonic function of density.

9.2 Mixture Thermodynamics

Consider a mixture of several components, having weight fractions w_k, $k=1,2,....$ The Helmholtz free energy of a mixture is given by the ideal mixing expression

$$A_{mix}(\rho, T, w_k) = \sum_k w_k A_k(\rho_k, T) - T\Delta S_{mix}, \tag{49}$$

where $A_k(\rho_k, T)$ is the free energy of component k at a density ρ_k, given by tabular EOS, and ΔS_{mix} is the entropy of mixing. As we will show below, ΔS_{mix} depends only on the composition of the system, not on density or temperature. Therefore, the energy and pressure of the mixture are given by

$$E_{mix}(\rho, T, w_k) = T^2 \frac{\partial}{\partial T}\left(\frac{A_{mix}}{T}\right)_\rho = \sum_k w_k E_k(\rho_k, T), \tag{50}$$

$$P_{mix}(\rho, T, w_k) = \rho^2 \left(\frac{\partial A_{mix}}{\partial \rho}\right)_T = \sum_k \lambda_k P_k(\rho_k, T), \tag{51}$$

$$\lambda_k = w_k(\rho^2/\rho_k^2)(\partial \rho_k/\partial \rho)_T. \tag{52}$$

Because ideal mixing involves no change in volume (at constant pressure and temperature), the densities must satisfy the additive volume condition,

$$1/\rho = \sum_k w_k/\rho_k, \text{ and } \sum_k \lambda_k = 1. \tag{53}$$

The above system of equations is now completed by choosing the densities so that the pressures P_k are all equal.[1]

1. One problem with this scheme is that the pressures of the individual components are not monotonic functions of density in the vapor-liquid coexistence region. This problem is handled in the following way, which is an improvement on that discussed in Sec. 10.2 of the PANDA manual. Maxwell constructions are put into the tables for the individual species, using a small finite slope of $(\partial P/\partial \rho)_T$ in the mixed phase region. A tension region is included in the mixture EOS by including a tension region for each component at low temperatures. The "pseudopressure" of each component is defined by shifting the pressure by a constant at low temperatures and fixing the densities by equating pseudopressures. This procedure is equivalent to equating the pressures while letting the mixture pressure go into tension. Finally, a small region of the EOS surface at low densities and temperatures, where the pseudopressure is not monotonic, is excluded from the calculation and replaced with an artificial construction like that discussed in Sec. 13.5 of the PANDA manual.

9.3 Entropy of Mixing

The entropy of mixing for an ideal solution is given by

$$\Delta S_{mix} = -(R/\bar{W})\sum_k n_k \ln n_k,\ \bar{W} = \sum_k n_k W_k. \text{ (complete miscibility)} \tag{54}$$

Here n_k and W_k are the mole fraction and molecular weight of component k, and $\bar{W}$ is the average molecular weight.[1] The mole fractions are related to the weight fractions by

$$n_k = w_k \bar{W}/W_k. \tag{55}$$

Equation (54) is valid only for a mixture in which all components are completely miscible. There are a number of situations in which this relation is incorrect. For example, metallic fluids are generally not miscible with molecular fluids. Because the entropy of mixing enters into the chemical equilibrium calculations, the assumption of complete miscibility can give erroneous results for the composition of the mixture in such cases.

In PANDA, Eq. (54) is replaced by the expression

$$\Delta S_{mix} = -(R/\bar{W})\sum_k p_k n_k \ln\left(p_k n_k / \sum_l p_l n_l\right). \text{ (partial miscibility)} \tag{56}$$

Here $p_k = 1$ for a completely miscible component, and $p_k = 0$ for a completely immiscible component. Examination of Eq. (56) shows that it describes a single homogeneous phase, consisting of miscible components, and several additional phases, one for each immiscible component. The present version of the model does not allow for more than one homogeneous mixture phase or for variations in miscibility with temperature and pressure. However, non-integral miscibility parameters, $0 < p_k < 1$, are allowed in the model and correspond to partial miscibility.[2]

1. The entropy of mixing expression in our 1972 EOS model contained an error. Applying Eq. (54) to a mixture of molecules and atoms, and defining f be the fraction of molecules that are dissociated, the entropy of mixing is found to be

$$\Delta S_{mix} = -(R/W)[(1-f)\ln(1-f) + 2f\ln 2f - (1+f)\ln(1+f)]$$

where W is the molecular weight. Equation (21) of Ref. [2] does not agree with this result. However, the error is small and has little effect on the predictions.

2. For a component with $p_k = 0.5$, half of the molecules would be soluble in the homogeneous phase, and the other half would form a separate phase.

9.4 Chemical Equilibrium

The molar composition of the mixture is determined by minimizing the Helmholtz free energy with respect to the mole fractions n_k at each density and temperature, subject to constraints that follow from the chemical formulas of the species. In setting up a problem, the user enters the molecular formula for each mixture component, along with some "initial" composition of the system, expressed in terms of mole or masses. The only requirement on the initial composition is that it be consistent with the overall elemental composition of the system. (PANDA does not require the specification of reaction paths among the components.)

PANDA then determines the chemical constraints in the following way. If $f(a, k)$ is the number of atoms of element a in a molecule of component k, it can be seen that the sum $f_a = \Sigma_k n_k f(a, k)$ for each element must be constant for all allowed chemical compositions of the mixture. PANDA determines the constants f_a from the molecular formulas and the initial composition and reduces the constraints to a linearly independent set of equations. If the number of constraints equals the number of chemical species, the mixture is inert, and the minimization procedure is skipped.

9.5 Application to Hydrogen

For the hydrogen isotopes, the above equations simplify when only molecular and atomic species are present. However, the full set of equations is required when additional species are considered, as in Sec. 9.6. (We reiterate that ionization is included in the atomic EOS, so electrons and nuclei are not included as separate species.)

Figure 6 shows the effect of dissociation on the deuterium Hugoniot. The solid, dashed, and dotted curves were calculated including dissociation but varying the miscibility parameter as discussed below. The dotdashed curve is the result when dissociation is not allowed. Experimental data from Refs. [4] and [7] are also shown for reference. (Squares are weighted averages of the data given in Ref. [7].)

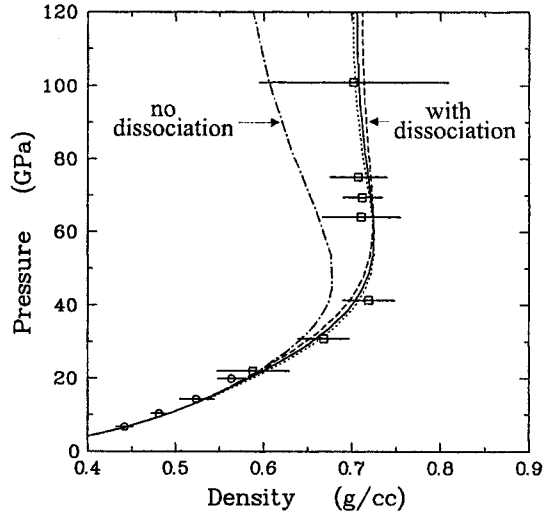

Fig. 6. Effect of dissociation on D_2 Hugoniot. Calculations with dissociation: solid line—p=0.75; dotted line—p=1.0; dashed line—p=0.5. Dotdashed line is calculation without dissociation. Experimental data: circles—gas gun [4]; squares—magnetic flyer [7].

The effect of miscibility was investigated by using the same parameter, $p_1 = p_2 = p$, for both molecules and atoms. One would not expect molecules and atoms to form a solution if the atomic fluid were metallic. As noted in Sec. 8.3, however, atomic H and D are insulating fluids at densities in the range of the principal Hugoniot. Therefore, the two species would be expected to be miscible in this regime. The three calculations shown in Fig. 6, with $0.5 \le p \le 1.0$, give very similar results, all within experimental uncertainty. We have elected to use $p = 0.75$ in the final version of the model because it gives slightly better agreement with the data at 20-30 GPa, where the effects of dissociation are just beginning to be important.

It might be thought that molecules and atoms would be less miscible at very high pressures, where the atoms are pressure-ionized and the fluid is metallic. If we use $p = 0.01$, the mixture model predicts a first-order phase transition between the molecular and atomic components at a pressure of about 500 GPa and temperatures below about 15,000K. However, analysis of the conductivity data appear to rule out immiscibility, even at high pressures, as shown in Sec. 10.8.

Figure 6 demonstrates that dissociation has a very significant effect on the Hugoniot in our model. When dissociation is not included, the Hugoniot density increases with pressure, has a maximum value of $4\rho_0$ at 50 GPa, then decreases at higher pressures to an asymptotic value of $3.3\rho_0$. As noted in Sec. 8, this behavior is due to the effects of anharmonicity and density on the vibrational and rotational degrees of freedom. When dissociation is included, the density still goes through a maximum value, $4.25\rho_0$ at 59 GPa, then decreases to the correct asymptotic value of $4\rho_0$ at high pressures. (Ionization also has an effect at high pressures, as we will show in Sec. 10.)

9.6 Other Chemical Species

All of the above results were obtained for a fluid phase consisting of only two chemical species—molecules and atoms. PIMC calculations showed that other chemical species can account up to 10% of the total molar concentration under certain conditions [26]. The more general version of the PANDA mixture model, which allows an unlimited number of mixture components, was used to investigate the importance of other species and their effects on the EOS.

PANDA offers a simplified analytic EOS option that can be used for sensitivity studies in lieu of the more sophisticated tabular EOS. (See Sec. 10.5 of the PANDA manual [34].) This option was used to model a deuterium mixture in which D_2^+, D_2^- and D^- ions are allowed to form in addition to D_2, D, D^+, and e^-. Those calculations showed that D^- was unimportant. However, the molecular ions D_2^+ and D_2^- were present in concentrations up to a few percent. The two ions appeared in almost identical concentrations, as expected from the balance equation $2D_2 \leftrightarrow D_2^+ + D_2^-$.

The analytic model is too simplistic to give reliable results at high densities. In order to investigate the effect of the molecular ions on the shock wave properties, we next constructed a tabular EOS for a "average" D_2^+/D_2^- ionic component. (This EOS is only preliminary, so we will not go into details in this report.) The model was similar to that for D_2, but the cold curve was computed from a formula that is appropriate for an ionic material. The vibration-rotation constants were taken from Ref. [78], and anharmonicity and density corrections were included; vibrational destabilization of the ions was found to occur at 1.2 g/cm^3.

The importance of the ionic component was found to depend strongly on the miscibility parameter. For complete miscibility, the maximum ion concentration was about 2% on the Hugoniot, with only a small effect on the Hugoniot curve itself. For low miscibility, virtually no ions were predicted to form.

We have elected to exclude the formation of D_2^+ and D_2^- ions in the present model. These species would probably be immiscible with either the molecules or atoms at low temperatures and high densities, but they would be miscible at high temperatures and low densities. Fortunately, they would have a small effect on the EOS in either case.

Further studies of additional chemical species may be needed. A satisfactory treatment of the ions would require extensions of the mixture model to deal with the effects of density and temperature on miscibility, which is beyond the scope of the present study. We defer these issues to another time.

9.7 Ionization State for the Mixture

The CONC PLOT option in PANDA can be used to compute the molar concentrations of molecules and atoms in the fluid. Because ionization is incorporated into the EOS for the atomic fluid, calculation of the number of ions and electrons involves some effort. The following procedure was used:

- At a given density and temperature, compute the pressure and the molar concentrations of molecules (X_2) and atoms (X_1). (Here molar concentration is defined as the number of moles per initial mole of molecules.)
- Compute the density of the atomic component from the pressure and temperature, using the ISOBAR option in PANDA.
- Compute the average ionization state $\langle z \rangle$ for the atomic component at that density and temperature, using Eq. (44).
- Compute the molar concentration of atomic ions from $X^+ = \langle z \rangle X_1$ and revise the atomic molar concentration by $X_1 \rightarrow X_1 - X^+$.
- Normalize the molar concentrations to unity.

This procedure was used for the calculations discussed in Secs. 10.7 and 10.8.

10. Results and Discussion

This section discusses the model predictions and compares them with experimental data, where available. (Note that some comparisions with experiment are also shown in Figs. 1 and 6.)

10.1 Phase Diagram

The phase diagrams of hydrogen and deuterium are shown in Fig. 7. The phase boundaries, shown by solid lines, were computed using the PANDA phase transition model and the EOS tables for the molecular solid, the atomic solid, and the two-component fluid phase. Results for the two materials are similar, but the transition from a molecular to an atomic solid occurs at a slightly higher pressure in hydrogen. The model does not predict a first-order transition boundary in the fluid region.

The molecular-atomic transition pressure is considerably higher than in our 1972 deuterium EOS—820 GPa compared with 220 GPa. The new result is consistent with experimental data that show the molecular solid still stable at 342 GPa [43]. The difference is due in part to the softer cold curve for the molecular solid. The calculated melting curves are in good agreement with the experimental melting data [58], shown by circles. (The lattice vibrational parameters were chosen to match the melting data, as noted in Sec. 5.1.) For comparison, loci for the principal Hugoniots are shown by dashed lines.

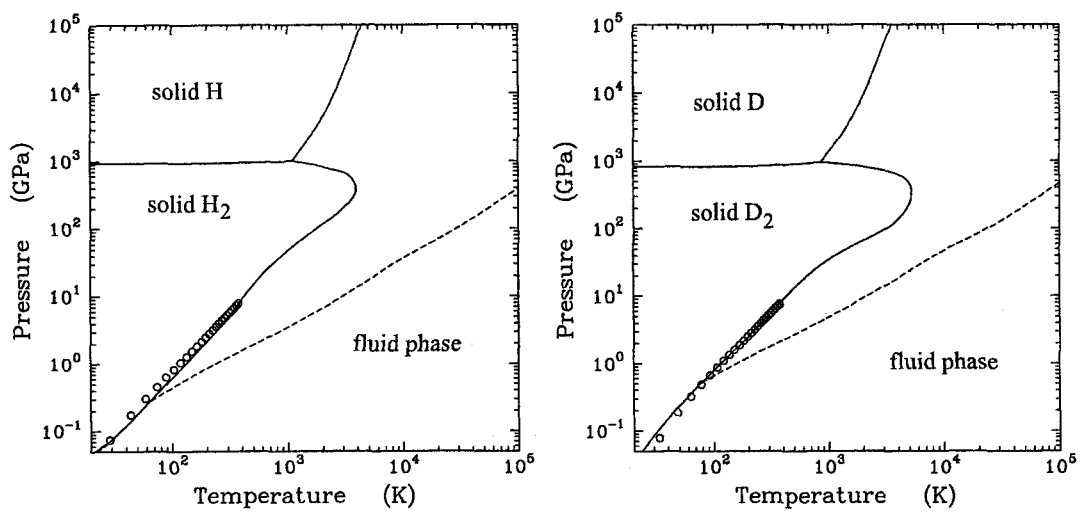

Fig. 7. Phase diagrams for hydrogen and deuterium. Solid curves are calculated phase boundaries. Circles are experimental melting data [58]. Dashed curves are Hugoniot loci.

Figure 8 compares the calculated vapor pressure and vapor-liquid coexistence curves with experimental data [84]. We have endeavored to obtain a good fit to the data in this regime, so that the final EOS table can be used to represent the cryogenic liquid—the initial state for many dynamic experiments. The quantum corrections to the fluid properties were especially important in matching the liquid densities on the coexistence curves.

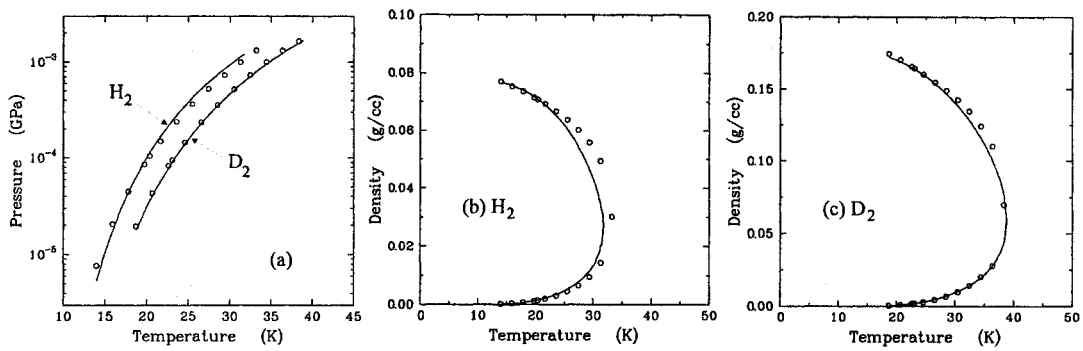

Fig. 8. Vaporization behavior of hydrogen and deuterium. Frame a shows vapor pressure vs. temperature for both isotopes. Frames b and c show the densities on the vapor-liquid coexistence boundary of H_2 and D_2, respectively. Solid curves are model calculations. Circles are experimental data [84].

10.2 Static Compression Data

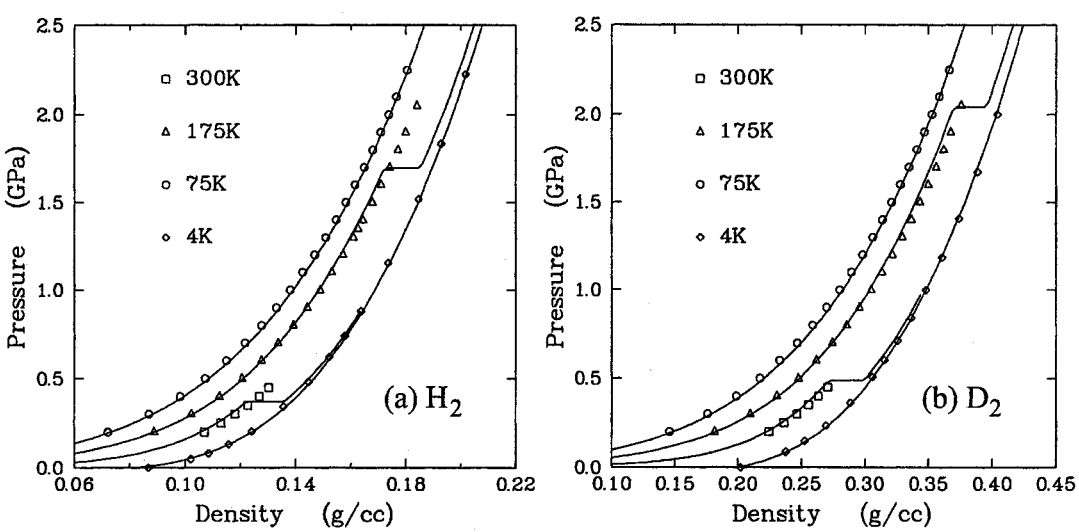

Fig. 9. Static compression of H_2 and D_2 at low temperatures and pressures. Solid curves are model calculations. Experimental data: circles—liquid[71]-[74]; squares—solid [51].

Figure 9 compares the model predictions with static compression data for both the liquid [71]-[74] and solid [51] phases of H_2 and D_2 at temperatures up to 300K and pressures up to 2.5 GPa. The quantum corrections are large in this regime, as in the vaporization region. The model gives good agreement with the data, except that it gives too low a melting pressure for hydrogen and too high a melting pressure for deuterium at low temperatures. (Also see Fig. 7.)

Figure 10 shows the sound speed of H_2 as a function of pressure at room temperature. The model calculation, shown by a solid line, agrees well with the data of Mills, et al. [71][72], and Duffy, et al. [86]. The discrepancy between the data of Brody, et al. [85], and the other measurements, has been attributed to approximations made in reducing the data [86].

The room temperature melting pressure is 5.3 GPa for hydrogen. Our model predicts a slightly lower value, 4.8 GPa. The low-pressure data in Fig. 10 lie in the liquid phase, the high pressure data in the solid phase. The model predicts a 1.2% increase in sound speed going from the liquid to the solid.

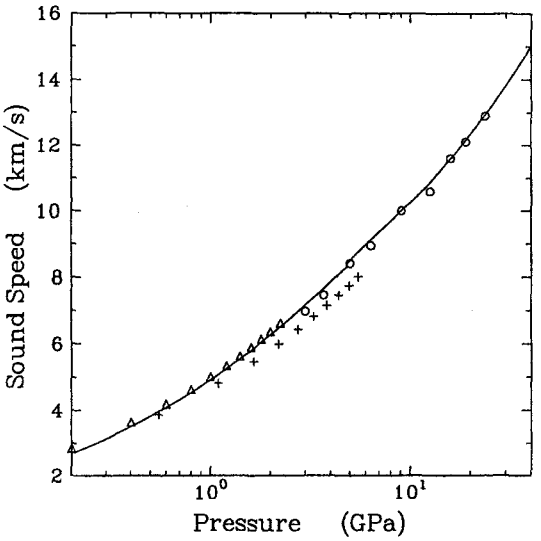

Fig. 10. Sound speed vs. pressure for H_2 at room temperature. Model calculation is shown by solid line. Experimental data—triangles [71][72], crosses [85], circles [86].

Our model calculations are compared with the pressure-density static compression data for hydrogen at high pressures in Fig. 1. To reiterate what was said in Sec. 4, the model curves are slightly stiffer than the experimental data of Ref. [52]. This discrepancy is necessary to give satisfactory agreement with shock wave data. It can be justified, at least in part, by the argument that the stiffer curve represents freely-rotating molecules, while the data correspond to molecules that are partly oriented.

10.3 Principal Hugoniot

The principal Hugoniot for deuterium is shown in Fig. 6, which also illustrates the effect of dissociation and the sensitivity to the mixture miscibility parameter. We show the deuterium Hugoniot again in Fig. 11, along with some additional experimental data and calculations. The model calculation for an initial liquid state (0.17 g/cm^3) is shown by a solid line. It is in good agreement with the experimental data from Refs. [4][6]-[9][37]. (We have not shown the Nova laser data [28]-[30], which we believe to be in error, as discussed in Sec. 1 and Appendix A.)

Detailed inspection of Fig. 11 shows that the Hugoniot for our model is slightly softer than the high-precision shock data reported by Nellis, et al. [4]. As noted in Sec. 4.1, we have not been able to obtain complete consistency between the shock wave and static data within the framework of our model. The stiffer cold curve that is required to pass through the shock wave data points is inconsistent with the static measurements. However, the discrepancy is small—just outside the reported error bars at the highest pressure point; we have not tried to determine what model improvements would be needed to eliminate it entirely.

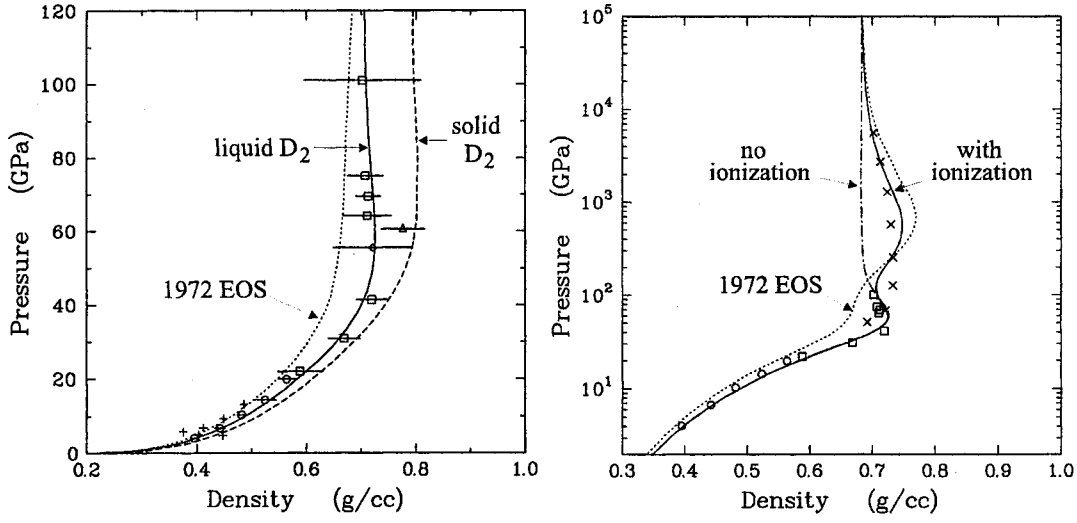

Fig. 11. Principal Hugoniot for deuterium. Model calculations: solid lines—liquid state; dashed line—solid state; dotted line—1972 model; dotdash line—liquid state, ionization turned off. Experimental data: initial liquid state—crosses [37], circles [4], squares [6]-[8], diamond [9]; initial solid state—triangle [10]. X's are PIMC calculations [25]

The dashed line in Fig. 11 is the calculated Hugoniot for an initial *solid* state (0.199 g/cm^3). The higher initial density results in higher shock densities, 5-10% depending on pressure. The model curve is well within the error bars of the single data point for the solid [10].

Although the Hugoniot density is close to the theoretical asymptotic value, $4\rho_0$, at 120 GPa, additional structure is observed when the calculation is extended to higher pressures. The density again increases with pressure above 120 GPa, reaches a maximum of $4.4\rho_0$ at 550 GPa, then decreases back to $4\rho_0$ at still higher pressures. This additional structure is due to the effects of ionization; it does not appear when ionization is turned off in the model, as seen by the dotted line in Fig. 11.[1] There are no experimental data at these high pressures, but the model calculation agrees quite well with the *ab initio* PIMC calculations of Militzer and Ceperley [25] in this regime. Experiments at pressures of 200 GPa or higher would be needed to observe the effects of ionization and test the model.

For comparison, Fig. 11 also shows the Hugoniot computed using the 1972 EOS (dotted line). The old model is not as accurate as the new one, although it displays the same qualitative behavior. The new EOS gives higher shock compressions at pressures below 120 GPa, in good agreement with the experimental data. The improvement is due to a combination of several factors—the high-order corrections in the liquid perturbation expansion, the softer zero-Kelvin curve for the molecular solid, the treatment of molecular vibrations and rotations, and the switch from equal densities to equal pressures in the mixture model. The improvements to the ionization equilibrium model lead to somewhat lower shock compressions at high shock pressures, in better agreement with the PIMC calculations.

The Hugoniot for hydrogen is shown in Fig. 12. It is more difficult to generate high pressures in H_2 than in D_2, because of its lower shock impedance. Therefore, most of the experimental measurements have focused on the heavier isotope. The model calculation agrees well with the experimental data that are available. It should be noted that the Hugoniots for the two isotopes do not scale in density because the initial state for H_2 corresponds to a larger molar volume than for D_2. As a result, H_2 has a higher Hugoniot temperature and lower compression than D_2 at the same pressure.

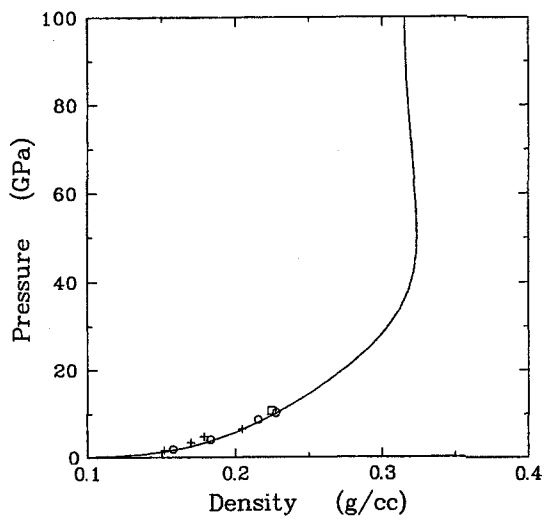

Fig. 12. Principal Hugoniot for hydrogen. Model calculation is shown by solid line. Experimental data: crosses [37], circles [4], squares [8]

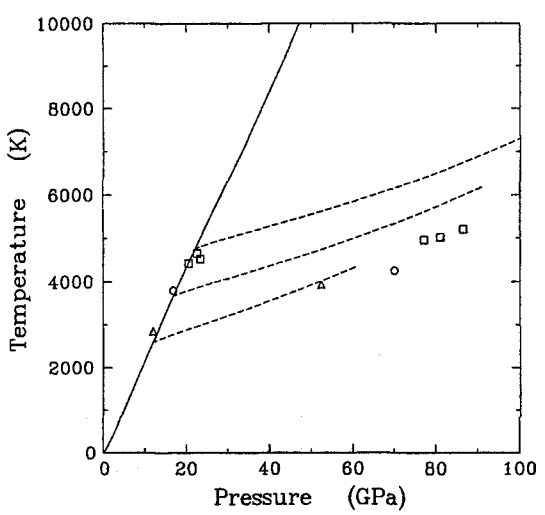

Fig. 13. Hugoniot temperature vs. pressure for deuterium. Solid line is principal Hugoniot, dashed lines are reflected Hugoniots. Data are from [87].

1. Although the calculations with and without ionization give the same Hugoniot *density* at high pressures, they do not give the same EOS. For example, the Hugoniot temperature is significantly higher when ionization is turned off.

Figure 13 shows the Hugoniot temperature as a function of pressure for deuterium. The principal Hugoniot for our model, shown by a solid line, is in good agreement with the experimental data of Holmes, et al. [87]. The reflected shock Hugoniots, shown by dashed lines, are discussed below.

10.4 Reflected Shocks

Reflected shocks are generated when a shock wave in a material of interest (the "sample") strikes a material of high impedance (the "anvil"). The reflected shock state in the sample can be determined from the measured shock velocity and EOS of the anvil, using the impedance matching technique.

Figure 14 compares our model calculations with reflected shock measurements in liquid deuterium, using aluminum and magnesium as anvil materials [4][37]. In this case, we have plotted the pressure of both the principal Hugoniot and reflected shocks as functions of particle velocity. The agreement is very good.

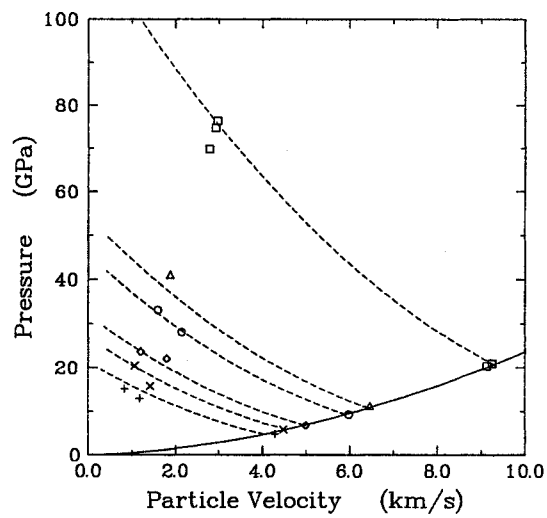

Fig. 14. Reflected shock curves for D_2. Model calculations: solid line—principal Hugoniot, dashed lines—reflected shocks. Experimental data are from Refs [4] and [37].

At very high pressures, questions about the EOS of the anvil arise and it may not be possible to make an accurate determination of the pressure and particle velocity by impedance matching. In this case, the experimentalist may prefer to plot the measured shock velocity in the anvil as a function of the initial shock velocity in the sample, thereby avoiding any assumption about the EOS of the anvil. Of course, it is still necessary to assume an EOS for the anvil in order to compare the theoretical model with the experimental data.

Figure 15 compares our model predictions with experimental data [8] for reflected shocks in liquid D_2, generated by aluminum (15a) and sapphire (15b) anvils. The *ab initio* calculations of Militzer, et al. [27], are also shown by diamonds in Fig. 15a. (The two sets of numbers shown correspond to the results of different numerical methods that were reported in the paper.) Our model gives good agreement with the experimental and numerical data. (We have not shown the Nike laser data [31][32], which we believe to be in error, as discussed in Sec. 1.)

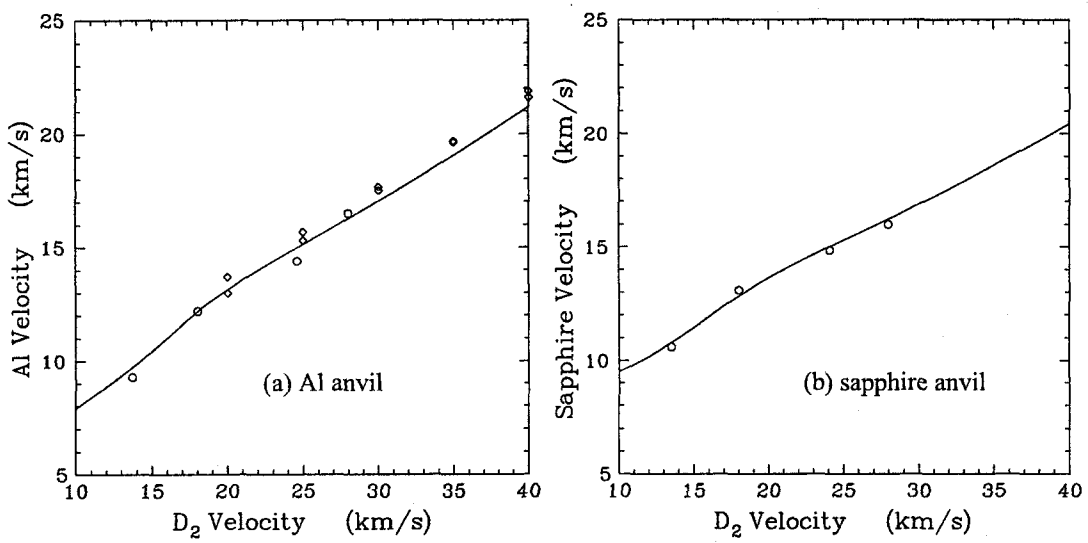

Fig. 15. Reflected shock experiments for deuterium. Frame a is for an Al anvil, frame b for a sapphire anvil. Solid line is model calculation. Circles are data of Knudson [8]. Diamonds in frame a are points computed using two different *ab initio* techniques [27].

The aluminum EOS used in our calculations was taken from Ref. [62] (EOS 3700 in the Sandia tabular EOS library). The aluminum Hugoniot has now been very well characterized by experiment at shock velocities up to 18 GPa, and there are also some data at considerably higher pressures [88]. The theoretical EOS is in excellent agreement with all the available data. Therefore, there is no reason to expect significant uncertainty due to the EOS of the anvil.

The sapphire Hugoniot, by contrast, is not well known in this regime. We have used an aluminum oxide EOS due to Barnes and Lyon [89] (EOS 7411 in the Los Alamos tabular EOS library) in our calculations. It should be noted that the experimental shock velocities for the aluminum and sapphire anvils are very close. Since the model calculations for aluminum agree with the data, any large discrepancy between the sapphire calculations and experiment would have to be attributed to the sapphire EOS, not the D_2 EOS.

Figure 13 compares our model predictions with principal Hugoniot and reflected shock temperature measurements of Holmes, et al. [87]. Our model gives good agreement with the principal Hugoniot and the reflected shock for a 12 GPa initial state. However, it does not agree with the measurements for reflected shocks from 17 and 22 GPa initial states. The data indicate only a slight increase in temperature on reshock. These experiments were initially cited as evidence that dissociation softens the EOS at high pressures. Models that agreed with these temperature measurements were also found to predict high shock compressions on the Hugoniot, like those obtained in the Nova laser experiments.

We have performed a number of sensitivity studies to determine what changes in the model are required to match the temperature data of Ref. [87]. We have not been able to find any way to match these data without destroying the agreement with other measurements. For example, it is possible to match the reshock temperatures by using a statistical weight on the atomic fluid to force dissociation. But that also softens the principal Hugoniot at pressures above 20 GPa and is totally inconsistent with the data of Refs. [6]-[10]. (Even so, it does not bring the predictions into agreement with the Nova laser data.)

A deficiency in our theoretical model cannot yet be ruled out, but further investigation of the temperature measurements is warranted. One possibility is that the low temperatures are due to cooling effects of the sapphire window used in the experiments [8]. The thermal conductivity of sapphire decreases with temperature—at *low* temperatures. However it increases again at high temperatures because of the radiative contribution [90]. It may be that previous analyses have underestimated the magnitude of window cooling effects.

10.5 Reverberation Experiments

Knudson, et al. [7][8], have used a shock reverberation technique to generate multiple shocks in deuterium at densities up to ten times liquid density. These experiments can be analyzed with the aid of the pressure-particle velocity (P-u_p) diagram shown in Fig. 16: A liquid D_2 sample is confined in a cell with an aluminum baseplate at the impact end and a sapphire window at the other end. The initial shock generates P-u_p state 1 on the principal Hugoniot of the sample. The shock traverses the sample and reflects off the sapphire window, producing P-u_p state 2, the intersection of the sapphire Hugoniot with the first D_2 reshock curve. The reflected shock then travels back through the sample and reflects off the Al baseplate, producing P-u_p state 3, the intersection of the second D_2 reshock curve with the reshock Hugoniot for the baseplate. The second reshock then traverses the sample a third time and arrives at the window.

Four times of arrival (TOA) are relevant to the experiment: t_1—TOA for the initial shock in the sample, t_2—TOA for the initial shock at the window, t_3—TOA for the first reshock at the baseplate, and t_4—TOA for the second reshock at the window. The initial transit time, $t_I = t_2 - t_1$, and the reverberation time for the first and second reshocks, $t_R = t_4 - t_2$, are determined in the experiment. The ratio of these two times is independent of the sample dimensions. It can be expressed in terms of the shock and particle velocities at state 1, 2, and 3 as follows.

$$t_R/t_I = U_{S1}(1 + U_{S2}/\mu_2 U_{S3})/\mu_1 U_{S2}, \tag{57}$$

where $\mu_1 = 1 - u_{p1}/U_{S1}$ and $\mu_2 = 1 - u_{p2}/U_{S2}$. Note that the shock and particle velocities in these expressions correspond to reference frames in which the sample is initially at rest before being shocked or reshocked.

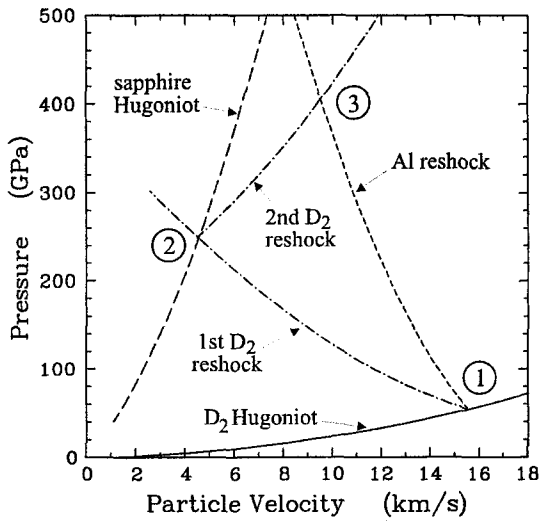

Fig. 16. Pressure-particle velocity diagram for reverberation experiment. See text for discussion of experiment.

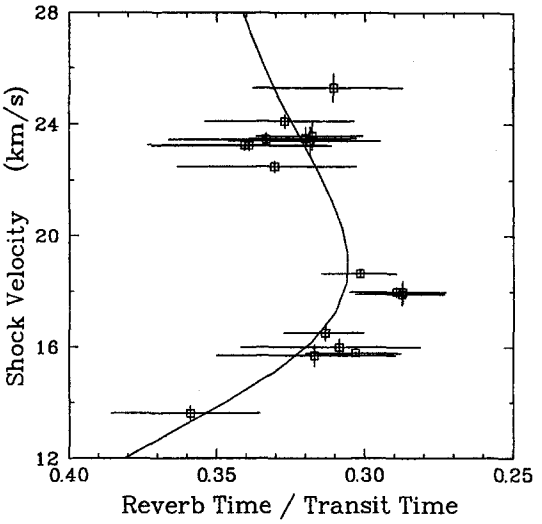

Fig. 17. Reverberation data for D_2. Model calculation is shown by solid line. Data are from Refs. [7][8]

Figure 17 compares our model calculations of the reverberation time ratio as a function of the initial deuterium shock velocity with the experimental data [7][8]. (Knudson, et al., plotted the time ratio on the abscissa in order to emphasize the correlation with the principal Hugoniot, and we have followed their example.) The same EOS for aluminum and sapphire were used as in the reshock calculations, Figs. 15.[1] The time ratio first decreases with increasing shock velocity, reaches a minimum at 19 km/s (45 GPa), and then increases with higher shock velocities. Our model is in good agreement with the data, both qualitatively and quantitatively.

Although the reverberation experiments generate very high density states in the deuterium, Knudson, et al., pointed out that the time ratios are most sensitive to the initial shock density. The reason for this fact is that the models they considered gave very similar results for the density and velocity jumps on reshocking, even though they gave quite different results for the initial shock density. Therefore, they used these measurements as independent evidence that the maximum density on the principal Hugoniot had to be about $4\rho_0$, in contrast to the much higher densities reported in the Nova laser experiments.

Since the reverberation technique generates such high densities, it would be interesting to compare directly to the shock and particle velocities of reshock states 2 and 3, in addition to the time ratio, if such measurements are feasible.

1. Sensitivity studies were made to investigate effects of uncertainty in the sapphire EOS. The predictions are surprisingly insensitive to reasonable variations in the sapphire model.

10.6 Comparison with Numerical Calculations

Figure 11 shows that our model agrees quite well with PIMC calculations of the deuterium Hugoniot [25] at pressures above 200 GPa. The agreement is poorer at low pressures. However, the PIMC results do not agree well with experiment in this regime, and it is evident that the method has numerical problems at low temperatures and high densities. Figure 15 shows that our model also agrees well with PIMC and DFT/PIMC calculations of the aluminum reshock experiments [27].

Militzer and Ceperley have also made extensive PIMC calculations of the hydrogen EOS at low densities, 0.001-0.15 g/cm^3, and temperatures from 5000-250,000K [26]. One of their stated purposes for this study was to provide a numerical test of the validity of chemical models. Figure 18 compares our model calculations with their calculations. We have also included the high density data for deuterium [26], with density and energy scaled according to atomic weight. The PIMC energies were shifted by +15.886 eV to give the same energy zero as our model, i.e., zero enthalpy for the molecular gas at room temperature and atmospheric pressure.

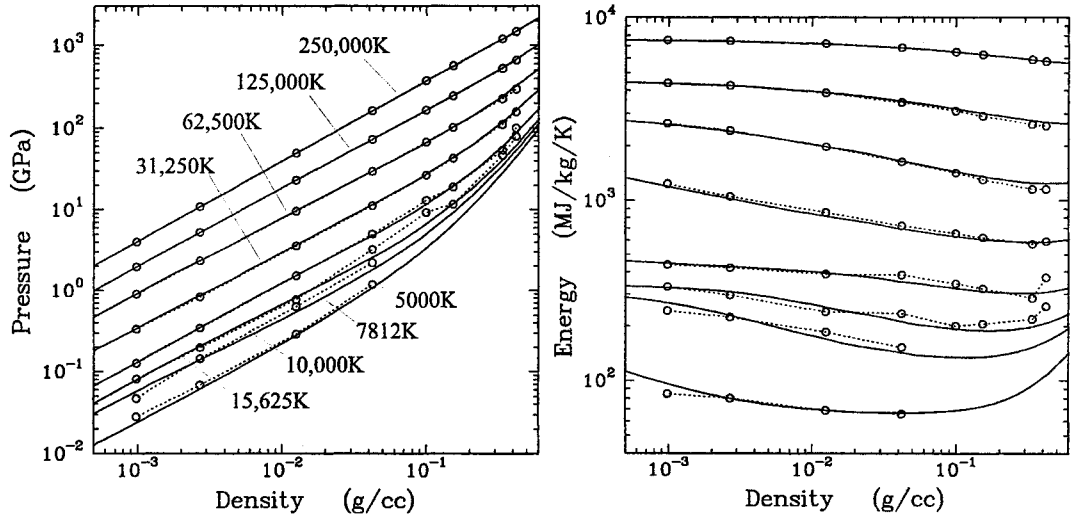

Fig. 18. EOS surface for hydrogen. Solid curves are model calculations. Circles connected by dotted lines are PIMC calculations [25][26]. PIMC energies were shifted to give the same energy zero as the model.

The agreement between our model and the PIMC results is generally very good. There are some discrepancies at the lowest temperatures, especially at high densities. As noted above, comparison between the Hugoniot data and the PIMC results shows that the method has numerical problems and is not exact. This conclusion is borne out by examination of the trends among the PIMC points. Therefore, we consider the agreement between our model and PIMC to be satis-

factory and do not regard the discrepancies as any indication of failure of the chemical picture of matter at high densities.

10.7 Dissociation and Ionization

Figure 19 compares our model predictions of dissociation and ionization in hydrogen with PIMC calculations for three isochores: frame (a) corresponds to an ion sphere radius $r_s = 2.6$ and density $\rho = 0.153$ g/cm^3, frame (b) to $r_s = 6.0$, $\rho = 1.25\times10^{-2}$, and frame (c) to $r_s = 14$, $\rho = 9.83\times10^{-4}$. Model calculations of the mole fractions of H_2 molecules, H_1 atoms, and H^+ ions are shown by solid, dashed, and dotdashed lines, respectively. The PIMC results [26] are shown by circles, squares, and triangles connected by dotted lines. (We have plotted the mole fractions as functions of pressure, rather than temperature, to be consistent with the discussion of the deuterium Hugoniot, below.)

In presenting their results for the mole fractions, Militzer and Ceperley cautioned that the PIMC method does not provide a completely rigorous and unique prescription for defining molecules, atoms and ions. They employed a "cluster analysis" that was based upon the proton-proton and proton-electron distances, along with certain energy criteria. However, they note that other definitions of atoms and molecules could give quantitatively different results.

Given these uncertainties, the agreement between our model and the PIMC results for the mole fractions of H_2 is quite satisfactory at all three densities. It should be noted that dissociation takes place over a wide range of pressure. The pressure corresponding to the onset of dissociation increases with increasing density, but complete dissociation always requires another order of magnitude increase in pressure.

By contrast, the PIMC results at all three densities predict the onset of ionization to occur at lower pressures and temperatures than our model.[1] This discrepancy is especially surprising at the lowest density, where the results of both theories should approach the ideal gas limit and there are fewer possibilities for error. This fact suggests that the cluster analysis overestimates the extent of ionization.

A simple check on the mole fractions from the cluster analysis can be made as follows. If the ideal gas approximation is valid, the pressure is proportional to the total number of free particles. Since dissociation doubles, and ionization quadruples, the number of free particles, the pressure for an ideal gas is given by

$$P = (X_2 + 2X_1 + 4X^+)RT\rho/W, \qquad (58)$$

1. Militzer and Ceperley also noted this discrepancy when comparing with the chemical model of Saumon and Chabrier [14].

where X_2, X_1, and X^+ are the mole fractions of molecules, atoms, and ions, respectively, and W is the molecular weight. This expression can be used to determine the weighted sum of mole fractions $X_2 + 2X_1 + 4X^+$ from the pressure.

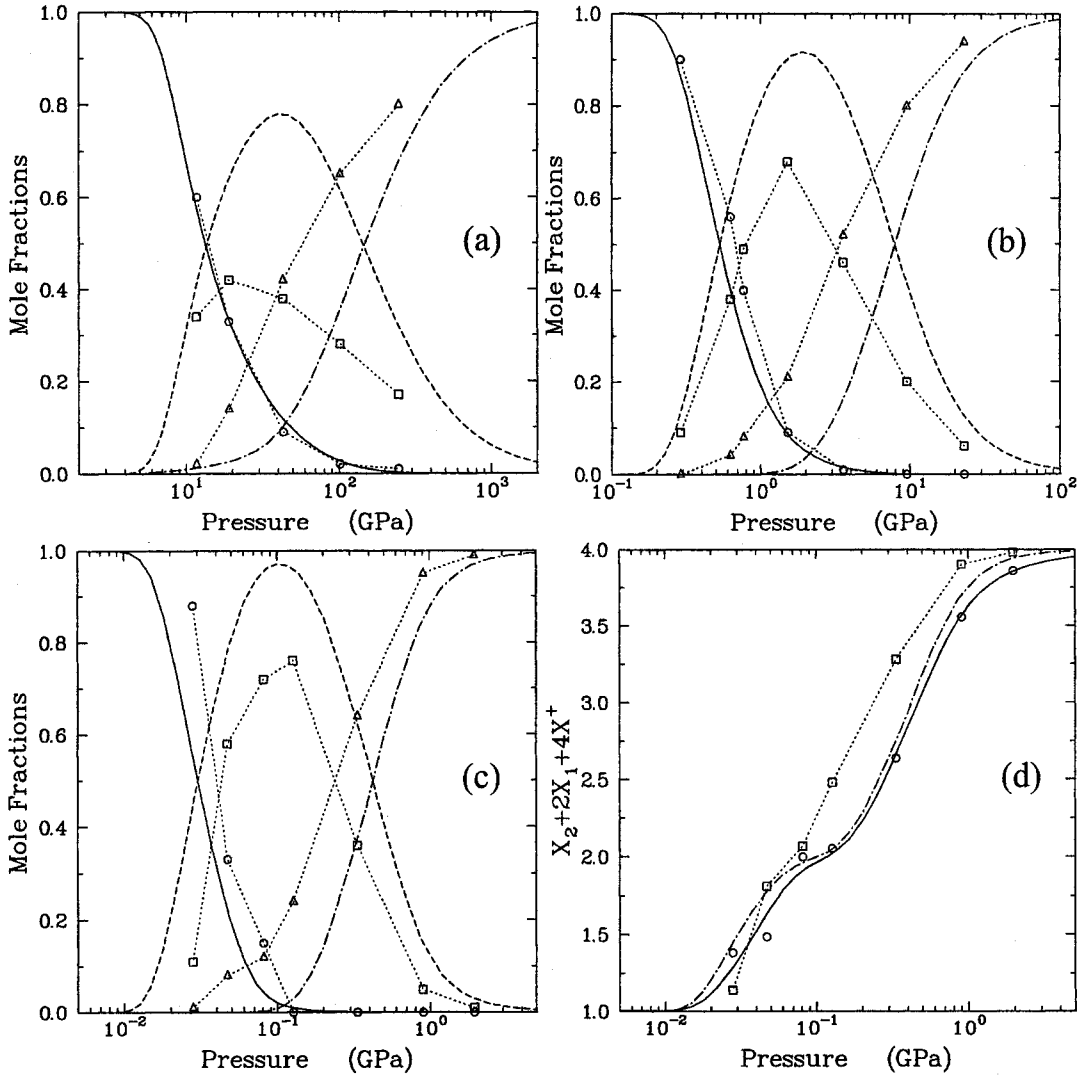

Fig. 19. Dissociation and ionization on hydrogen isochores: (a) $r_s = 2.6$; (b) $r_s = 6.0$; (c) $r_s = 14$. In frames (a)-(c): mole fraction of H_2—solid curve is model, circles connected by dotted lines are PIMC calculations [26]; mole fraction of H_1—dashed curve is model, squares are PIMC; mole fraction of H^+—dotdashed curve is model, triangles are PIMC. Frame (d) shows weighted sums of mole fractions at $r_s = 14$, computed as discussed in text; solid and dotdashed curves are model calculations, circles and squares are PIMC results.

Figure 19d shows the weighted mole fraction sum vs. pressure for the lowest density, $r_s = 14$, $\rho = 9.83\times10^{-4}$, where the ideal gas approximation should be most accurate. The circles were computed from Eq. (58), using the PIMC pressures, and the

squares were computed by direct summation of the mole fractions from the cluster analysis. The cluster analysis gives a significantly higher value for the weighted sum at pressures above 0.1 GPa, a strong indication that it overestimates the extent of ionization.

The same analysis was made on our model calculations, and the results are also shown in Fig. 19d. There is good agreement between the weighted mole fraction sum obtained from the pressure (solid line) and that obtained by direct summation of the mole fractions (dotdashed line). Moreover, both model curves agree well with the PIMC pressure results.

Based upon the above arguments, we believe that the discrepancy between our ionization predictions and the PIMC results is most likely due to uncertainties in the cluster analysis, not to errors in our chemical model.

Figure 20 shows our model calculations of dissociation and ionization along the deuterium Hugoniot. The onset of dissociation occurs at a pressure near 25 GPa, which coincides with the softening observed in the principal Hugoniot, Fig. 11. Dissociation is essentially complete at 300 GPa. This result is consistent with the calculations shown in Fig. 11, which indicate that dissociation occurs over an order of magnitude range in pressure.

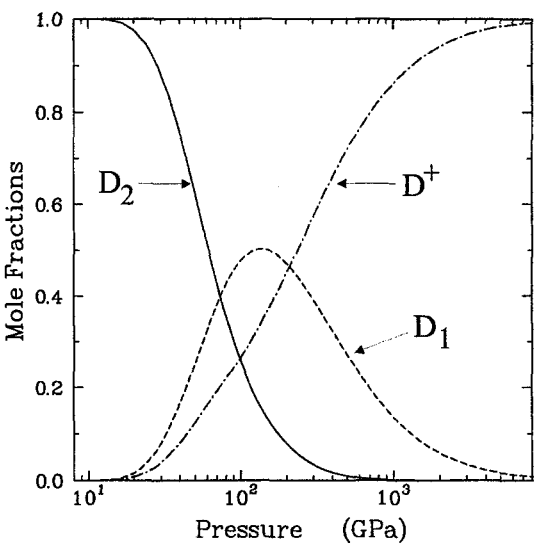

Fig. 20. Dissociation and ionization on deuterium Hugoniot.

Ionization begins at a lower pressure, relative to dissociation, than in Fig. 11, with the result that the atomic mole fraction never exceeds 0.5. This behavior is due to lowering of the ionization potential, Eq. (45), which favors ionization at high densities. The model and PIMC results shown in Fig. 11 also indicate this trend toward lower atomic mole fractions at higher densities. At still higher densities, above about 0.9 g/cm^3, atomic deuterium is pressure-ionized, and the mole fraction of D drops to zero.

10.8 Conductivity Experiments

Electrical conductivity measurements on shocked H_2 and D_2 [5][91][92] show that the conductivity increases with both temperature and pressure. This observation correlates with the increase in ionization with temperature and pressure predicted

by our model. In this section, we endeavor to make a rough quantitative comparison between the conductivity data and our ionization predictions.

The experiments discussed in Refs. [5], [91], and [92] were carried out in regions of temperature and pressure where our model predicts relatively low levels of dissociation and ionization. A rigorous theory of electrical conductivity in this regime is beyond the scope of the present study. However, the model of Lee, More, and Zimmerman (LMZ) [83][93]-[95] provides a starting point. We have modified the LMZ model to use our ionization state and melting curve but have used the default values for all other model parameters. Details are given in Appendix B.

Before presenting the results, we emphasize that our calculations are very crude and are not intended to serve in place of a full theoretical treatment of the electrical conductivity. We do not seek to predict the conductivity or even to fit the data. We only want to see if our ionization predictions are reasonably consistent with these data. The LMZ model cannot be expected to give a highly accurate description of the conductivity in this regime, where ionization levels are low and molecules predominate. But we felt that it was preferable to use an elementary conductivity model for our purpose than to ignore the issue altogether.

Nellis, et al. [91], measured the electrical conductivity of deuterium on the principal Hugoniot, in the range 13-20 GPa, corresponding to temperatures in the range 2200-4500K. Their data, shown as squares in Fig. 21, exhibit a rapid rise in conductivity with pressure due to shock heating. Our model predicts the ionization to increase from 2×10^{-4} electrons/atom at 13 GPa to 4×10^{-3} at 20 GPa, consistent with the observed trend. The dotted curve in Fig. 21 was computed using our modified version of the LMZ model. It is in rough agreement with both the magnitude of the conductivity and its dependence on pressure, indicating that our EOS model predicts reasonable levels of ionization in this regime.

Weir, et al. [5], used a multiple-shock technique to investigate the electrical conductivity of hydrogen and deuterium at pressures in the range 93-180 GPa and temperatures in the range 2000-5000K. Hypervelocity impactors were used to shock liquid samples contained between two Al_2O_3 plates. The pressure in the sample reverberates up to the first shock pressure in the Al_2O_3, resulting in high pressures but much lower temperatures and much higher compressions than would be obtained by a single shock. The conductivity was observed to increase by four orders of magnitude from 93 to 140 GPa and was essentially constant from 140-180 GPa. The high-pressure value, 2000 $(\text{ohm-cm})^{-1}$, is comparable to that for metals at high temperature. Fortov, et al. [92], also reported reverberation experiments in the same regime and obtained results close to those of Weir, et al.

The data of Weir, et al., are shown by circles (H_2) and triangles (D_2) in Fig. 21. Note that the reverberation experiments cover nearly the same temperature range as the Hugoniot experiments, even though the pressures are much higher. Com-

parison of the Hugoniot and reverberation data shows that ionization increases with pressure at a constant temperature, as predicted by our model.

In order to compare with the reverberation data, we made hydrocode simulations of the experiments, using our EOS to determine the densities and temperatures of the final states of the H_2 and D_2 samples at various initial shock states in the Al_2O_3. Using these final states, we find that the ionization increases from 3×10^{-4} electrons/atom to 3×10^{-2} in H_2 and from 2×10^{-3} to 9×10^{-2} in D_2 over the pressure range from 90 to 180 GPa. (H_2 undergoes less ionization than D_2 because it has a lower density and so undergoes smaller pressure increments and less shock heating during ring-up to the final state.)

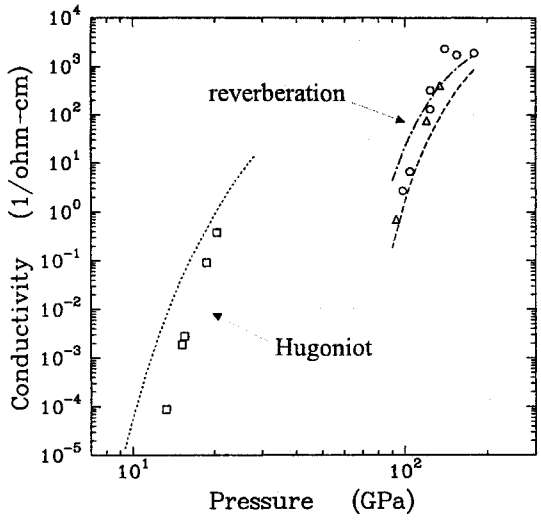

Fig. 21. Electrical conductivity of shocked hydrogen and deuterium. Experiment: squares—D_2 Hugoniot [91], triangles—D_2 reverberation [5], circles—H_2 reverberation [5]. Calculations: dotted line—D_2 Hugoniot, dotdashed line—D_2 reverberation, dashed line—H_2 reverberation.

The conductivities for the reverberation experiments, calculated using the modified LMZ model, are shown by the dashed line (H_2) and the dotdashed line (D_2) in Fig. 21. They are in rough agreement with the data and also predict the large difference between the Hugoniot and reverberation experiments. However, the experimental data do not exhibit a significant difference between H_2 and D_2 as do the calculations. This fact suggests problems in the conductivity model, rather than in the ionization predictions, since any reasonable EOS model should predict less ionization in H_2 than D_2 under the conditions of the reverberation experiments.

One complication in the interpretation of these experiments is that our phase diagram (Fig. 7) predicts that D_2 will cross over into the molecular solid regime during ring-up at pressures below 117 GPa. H_2 has a lower melting pressure than D_2 and is predicted to remain in the fluid range. It does not seem likely that solidification would occur on the short time scale (~ 0.2 μsec) that it takes for the liquid to reach the final state. (Solidification was not included in the hydrocode simulations.) However, this issue may merit further consideration.

The fact that the calculations are in general agreement with the observed trends in the data shows that there are no gross deficiencies in our ionization model. However, there is clearly room for improvement. Some of the discrepancies with experiment could be due to the calculated ionization state, but they are much more

likely to be due to deficiencies in the conductivity model. In fact, it is somewhat surprising that such a simple conductivity model gives as good agreement as it does. It would be easy to improve the agreement by adjusting the LMZ parameters, but we have not done that here in order to avoid clouding the issue.

The reverberation experiments also give some insight into the nature of miscibility between the molecular and atomic components of the mixture at high pressures. The above calculations were made using a miscibility parameter of 0.75 (Sec. 9.3), which does not predict any first-order transition from a molecular to a metallic fluid. If the miscibility parameter is dropped to 0.01, making the two components immiscible, the model does predict a first-order transition at temperatures below about 15,000K. However, the immiscible model does not predict significant dissociation or ionization at pressures below 500 GPa, and that is inconsistent with the conductivity data. Therefore, we believe that the higher miscibility parameter is appropriate even at high pressures.

10.9 Implications for Planetary Models

The EOS of hydrogen plays a key role in modeling the "giant planets," Jupiter and Saturn, which consist primarily of hydrogen and a smaller amount of helium. (See Refs. [96]-[98] and references cited therein.) The simplest planetary model assumes that all points in the planet's interior lie on an adiabat (isentrope) passing through a given temperature-pressure state at the surface. The problem is further simplified if the composition, e.g., the helium abundance, is assumed to be constant throughout the interior. Having calculated the isentrope from the EOS, one can solve for pressure and density as a function of radius, requiring that the mass distribution give hydrostatic equilibrium in the planet's own gravitational field. More complicated models consider variations in the helium abundance along the isentrope and deviations from isentropic conditions.

We have used our new hydrogen EOS, together with a preliminary helium EOS, to make calculations of the structures of Jupiter and Saturn. These calculations are too preliminary to be presented here, and a full discussion of all the issues involved is beyond the scope of this report. However, there are three points that should be mentioned.

First, much of the work in the literature on Jupiter and Saturn has employed EOS models that include a plasma phase transition (PPT) [14]. The existence of a PPT not only affects the thermodynamic properties; it has also been used to justify changes in the helium abundance at the phase boundary [98]. Our EOS model does not predict a PPT, a result that is consistent with the experimental data and *ab initio* calculations currently available. A first-order transition can be obtained by using a smaller miscibility parameter, but the results are inconsistent with the conductivity data, as noted above. Hence there is little reason to believe that a PPT

exists in hydrogen. The absence of a PPT will require reevaluation of previous Jupiter and Saturn models.

Second, our new EOS predicts a higher pressure for the transition from molecular to atomic hydrogen than has been used in previous work. This result, which is consistent with the latest static measurements on the molecular solid, leads to a smaller metallic core for the Jovian planets. Previous models of Jupiter predicted a PPT to a metallic liquid at about 200 GPa, resulting in a metallic core for distances less than 80% of the outer radius [98]. Our model predicts dissociation to occur over the pressure range 200-1000 GPa on the Jupiter isentrope, the molecular and atomic components having equal concentrations at about 500 GPa. Taking 500 GPa as the "boundary" of the metallic core, the corresponding radius would be about 65% of the outer radius of Jupiter.

Finally, our new and softer EOS gives different results for the abundance of heavy elements present in the planetary interiors. The stiffer the EOS, the more heavy elements are needed to account for the mass of the planet. Most previous models have required a dense central core of rock or ice to account for the mass. Preliminary calculations indicate that our new EOS model does not require a dense core for Jupiter. The helium abundance and the adiabatic hypothesis may also need to be reevaluated.

11. Conclusions and Recommendations

The present study demonstrates that the basic approach used in our 1972 deuterium EOS—the "chemical model"—is fundamentally sound. However, the model has been significantly improved by incorporating new developments in the theories of liquids, ionization equilibrium, and mixtures that have taken place during the last thirty years. Careful attention to certain details, such as the treatment of molecular vibrations and rotations, has also proven to be important.

A recurring issue throughout this work is the validity of the chemical picture of matter, especially at high densities. In recent years, some have argued that advances in *ab initio* numerical computation have exposed serious flaws in chemical models and are making them obsolete. We do not agree with this view.

Ab initio methods are unquestionably valuable tools for developing and testing models, and they will certainly become even more important in the future. However, they are not yet capable of sufficient accuracy to supplant other EOS modeling options. Increased computing power will not remove all their limitations; there are also a number of theoretical issues to be solved, as noted in Sec. 2.

When the numerical methods do become capable of the desired accuracy, it will be natural to rely on them more than can be done at present. Even then, chemical models will still be needed to understand the phenomena that control material behavior, much as they are used for interpreting experimental data.

Of course, different chemical models employ different approximations; one should not expect all chemical models to predict similar results. In particular, a number of models have been developed to match the Nova/Nike laser measurements—data that we now believe to be erroneous. There are several significant differences between those models and ours; they typically use more approximate theories to treat the atomic fluid and ignore anharmonicity and density effects on the molecular vibrations and rotations. The failure of one chemical model does not necessarily imply the failure of another.

Experience has shown that no EOS model is ever the final answer, that refinements to the theory are always possible and desirable. In the present case, more work will be needed to improve agreement between the static and shock wave data at high pressures. Questions remain about the zero-Kelvin isotherms for the atomic solid. The discrepancy between our model and the reflected shock temperature measurements needs investigation, including analysis of window cooling effects. Further studies of the effects of molecular ions (H_2^+/H_2^-) and other chemical species on the EOS may prove to be useful. Finally, it will be interesting to apply our EOS to models of the giant planets.

References

[1] G. I. Kerley, "A New Model of Fluids," Los Alamos Scientific Laboratory report LA-4760 (1971).

[2] G. I. Kerley, "A Theoretical Equation of State for Deuterium," Los Alamos Scientific Laboratory report LA-4776 (1972).

[3] G. I. Kerley, "Equation of State and Phase Diagram of Dense Hydrogen," Phys. Earth Planet. Interiors 6, 78-82 (1972).

[4] W. J. Nellis, A. C. Mitchell, M. van Thiel, G. J. Devine, R. J. Trainor, and N. Brown, "Equation-of-State Data for Molecular Hydrogen and Deuterium at Shock Pressures in the Range 2-76 GPa (20-760 kbar)." J. Chem. Phys. 79, 1480-1486 (1983).

[5] S. T. Weir, A. C. Mitchell, and W. J. Nellis, "Metallization of Fluid Molecular Hydrogen at 140 GPa (1.4 Mbar)," Phys. Rev. Lett. 76, 1860-1863 (1996).

[6] M. D. Knudson, D. L. Hanson, J. E. Bailey, C. A. Hall, J. R. Asay, and W. W. Anderson, "Equation of State Measurements in Liquid Deuterium to 70 GPa," Phys. Rev. Lett. 87, 225501 (2001).

[7] M. D. Knudson, D. L. Hanson, J. E. Bailey, C. A. Hall, and J. R. Asay, "Use of a Wave Reverberation Technique to Infer the Density Compression of Shocked Liquid Deuterium," Phys. Rev. Lett. 90, 035505 (2003).

[8] M. D. Knudson, Sandia National Laboratories, personal communication. The experiments of Knudson, et al., were performed on samples with an initial density of 0.167 g/cm^3, while a density of 0.170 g/cm^3 has been assumed in the calculations shown in this report. Agreement with their experimental data is slightly better when the lower initial density is used.

[9] R. D. Trunin, et al., in Proceedings of 6th Zababakhin Scientific Readings (to be published). Also see citations in Refs. [7] and [33].

[10] S. I. Belov, G. V. Boriskov, A. I. Bykov, R. I. Il'kaev, N. B. Luk'yanov, A. Ya. Matveev, O. L. Mikhailova, V. D. Selemir, G. V. Simakov, R. F. Trunin, I. P. Trusov, V. D. Urlin, V. E. Fortov, and A. N. Shuikin, "Shock Compression of Solid Deuterium," JETL Lett. 76, 433-435 (2002).

[11] H.-K Mao and R. J. Hemley, "Ultrahigh-Pressure Transitions in Solid Hydrogen," Rev. Mod. Phys. 66, 671-692 (1994).

[12] E. G. Maksimov and Y. I. Shil, "Hydrogen at High Pressure," Phys. Usp. Fiz. Nauk 42, 1121-1138 (2000).

[13] M. Ross, F. H. Ree, and D. A. Young, "The Equation of State of Molecular Hydrogen at a Very High Density," J. Chem. Phys. 79, 1487 (1983).

[14] D. Saumon, G. Chabrier, and H. M. Van Horn, "An Equation of State for Low-Mass Stars and Giant Planets," Astrophys. J., Suppl. Ser. 99, 713-741 (1995).

[15] J. H. Gardner and G. Hazak, "A Simple Model for Dissociation of Diatomic Molecules," Naval Research Laboratory Report NRL/MR/6440-97-7967 (1997).

[16] M. Ross, "Linear Mixing Model for Shock-Compressed Liquid Deuterium," Phys. Rev. B 58, 669-667 (1998).

[17] D. A. Young, "A New Global Hydrogen Equation of State Model," in Shock Compression of Condensed Matter - 1999, edited by M. D. Furnish, L. C. Chhabildas, and R. S. Hixson (AIP Conference Proceedings 505, 2000) pp. 53-56.

[18] B. I. Min, H. J. F. Jansen, and A. F. Freeman, "Structural Properties, Superconductivity, and Magnetism of Metallic Hydrogen," Phys. Rev. B 30, 5076-5083 (1984).

[19] D. M. Ceperley and B. J. Alder, "Ground State of Solid Hydrogen at High Pressures," Phys. Rev. B 36, 2092-2106 (1987).

[20] T. W. Barbee III, A. Garcia, M. L. Cohen, and J. L. Martins, "Theory of High-Pressure Phases of Hydrogen," Phys. Rev. Lett. 620, 1150-1153 (1989).

[21] V. Natoli, R. M. Martin, and D. M. Ceperley, "Crystal Structure of Atomic Hydrogen," Phys. Rev. Lett. 70, 1952-1955 (1993).

[22] T. J. Lenosky, J. D. Kress, and L. A. Collins, "Molecular-Dynamics Modeling of the Hugoniot of Shocked Liquid Deuterium," Phys. Rev. B 56, 5164-5169 (1997).

[23] T. J. Lenosky, S. R. Bickham, J. D. Kress, and L. A. Collins, "Density-Functional Calculation of the Hugoniot of Shocked Liquid Deuterium," Phys. Rev. B 61, 1-6 (2000).

[24] G. Galli, R. Q. Hood, A. U. Hazi, and F. Gygi, "*Ab Initio* Simulations of Compressed Liquid Deuterium," Phys. Rev. B 61, 909-912 (2000).

[25] B. Militzer and D. M. Ceperley, "Path Integral Monte Carlo Calculation of the Deuterium Hugoniot," Phys. Rev. Lett. 85, 1890-1893 (2000).

[26] B. Militzer and D. M. Ceperley, "Path Integral Monte Carlo Simulation of the Low-Density Hydrogen Plasma," Phys. Rev. E 63, 066404, 1-10 (2000).

[27] B. Miltizer, D. M. Ceperley, J. D. Kress, J. D. Johnson, L. A. Collins, and S. Matzevet, "Calculation of a Deuterium Double Shock Hugoniot from Ab Initio Simulations," Phys. Rev. Lett. 87, 275502 (2001).

[28] L. B. Da Silva, P. Celliers, G. W. Collins, K. S. Budil, N. C. Holmes, T. W. Barbee Jr., B. A. Hammel, J. D. Kilkenny, R. J. Wallace, M. Ross, R. Cauble, A. Ng, and G. Chiu, "Absolute Equation of State Measurements on Shocked Liquid Deuterium up to 200 GPa (2 Mbar)," Phys. Rev. Lett. 78, 483-486 (1997).

[29] G. W. Collins, P. Celliers, L. B. Da Silva, R. Cauble, D. Gold, M. Foord, K. S. Budil, R. Stewart, N. C. Holmes, M. Ross, B. A. Hammel, J. D. Kilkenny, R. J. Wallace, and A. Ng, "Equation of State Measurements of Hydrogen Isotopes on Nova," Phys. Plasmas 5, 1864-1869 (1998).

[30] G. W. Collins, L. B. Da Silva, P. Celliers, D. Gold, M. Foord, R. J. Wallace, A. Ng, S. V. Weber, K. S. Budil, and R. Cauble,, "Measurements of the Equation of State of Deuterium at the Insulator-Metal Transition," Science 281, 1178-1181 (1998).

[31] A. N. Mostovych, Y. Chan, T. Lehecha, A. Schmitt, and J. D. Sethian, "Reflected Shock Experiments on the Equation-of-State Properties of Liquid Deuterium," Phys. Rev. Lett. 85, 3870-3873 (2000).

[32] A. N. Mostovych, Y. Chan, T. Lehecha, L. Phillips, A. Schmitt, and J. D. Sethian, "Reflected Shock Experiments on the Equation-of-State Properties of Liquid Deuterium at 100-600 GPa (1-6 Mbar)," Phys. Plasmas 8, 2281-2286 (2001).

[33] W. Nellis, "Shock Compression of Deuterium Near 100 GPa Pressures," Phys. Rev. Lett. 89, 165502-1,4 (2002).

[34] G. I. Kerley, "User's Manual for PANDA II: A Computer Code for Calculating Equations of State," Sandia National Laboratories report SAND88-2291, 1991.

[35] G. I. Kerley, "Perturbation Theory and the Thermodynamic Properties of Fluids. I. General Theory," J. Chem. Phys. 73, 478-486 (1980).

[36] G. I. Kerley, "Perturbation Theory and the Thermodynamic Properties of Fluids. II. the CRIS Model," J. Chem. Phys. 73, 478-486 (1980).

[37] R. D. Dick and G. I. Kerley, "Shock Compression Data for Liquids. II. Condensed Hydrogen and Deuterium," J. Chem. Phys. 79, 1480-1486 (1983).

[38] G. I. Kerley, "A Model for the Calculation of Thermodynamic Properties of a Fluid," in Molecular-Based Study of Fluids, (ACS, Wash., D.C., 1983), pp 107-138.

[39] G. I. Kerley, "Equations of State and Gas-Gas Phase Separation in Soft Sphere Mixtures," J. Chem. Phys. 91, 1204 (1989).

[40] G. I. Kerley, "Theoretical Model of Explosive Detonation Products: Tests and Sensitivity Studies," in Proceedings of the Ninth Symposium (International) on Detonation, edited by W. J. Morat, OCNR 113291-7 (Office of the Chief of Naval Research, 1990), pp. 443-451.

[41] G. I. Kerley, "Theory of Ionization Equilibrium: An Approximation for the Single Element Case," J. Chem. Phys. 85, 5228-5231 (1986).

[42] G. I. Kerley and L. C. Chhabildas, "Multicomponent-Multiphase Equation of State for Carbon," Sandia National Laboratories report SAND2001-2619, 2001.

[43] C. Narayana, H. Luo, J. Orloff, and A. L. Ruoff, "Solid Hydrogen at 342 GPa: No Evidence for an Alkali Metal," Nature 393, 46-49 (1998).

[44] M. Born and J. R. Oppenheimer, Ann. d. Phys. 84, 457 (1927). This principle is discussed in many textbooks on quantum mechanics. For example, see L. Pauling and E. B. Wilson, Jr., Introduction to Quantum Mechanics (McGraw-Hill, NY, 1935) p 260.

[45] N. D. Mermin, "Thermal Properties of the Inhomogeneous Electron Gas," Phys. Rev. 5A, 1441-1443 (1965).

[46] M. Ross and L. H. Yang, "Computer Simulations for Shock Compressed Liquid Deuterium: Failure of Density Functional Theory-Molecular Dynamics," Phys. Rev. B 64, 174102 (2001).

[47] J. W. Stewart, J. Phys. Chem. Solids 1, 146 (1956); J. W. Stewart, J. Phys. Chem. Solids 29, 748 (1968).

[48] D. A. Liberman, "Equation of State of Molecular Hydrogen at High Pressure," Los Alamos National Laboratory report LA-4727-MS (1971). Later published in Int. J. Quantum Chem. Symp. No. 10, 297-303 (1976).

[49] G. A. Neece, F. J. Rodgers, and W. G. Hoover, J. Comp. Phys. 7, 621 (1971).

[50] J. Bardeen, J. Chem. Phys. 6, 367 (1938).

[51] M. S. Anderson and C. A. Swenson, "Experimental Compressions for Normal Hydrogen and Normal Deuterium to 25 kbar at 4.2 K," Phys. Rev. B 10, 5184-5191 (1974).

[52] P. Loubeyre, R. LeToullec, D. Hausermann, M. Hanfland, R. J. Hemley, H. K. Mao, and L. W. Finger, "X-ray Diffraction and Equation of State of Hydrogen at Megabar Pressures," Nature 383, 702-704 (1996).

[53] D. Saumon and H. M. van Horn, "Toward an Improved Pure Hydrogen EOS for Astrophysical Applications," NATO ASI Ser., Ser. B 1987, Vol. 154, Strongly Coupled Plasma Physics, 173-177.

[54] I. F. Silvera and V. V. Goldman, "The Isotopic Intermolecular Potential for H2 and D2 in the Solid and Gas Phases," J. Chem. Phys. 69, 4209-4123 (1978).

[55] M. Ross and A. K. McMahan, "Comparison of Theoretical Models for Metallic Hydrogen," Phys. Rev. B 13, 5154-5157 (1976).

[56] D. M. Straus and N. W. Ashcroft, "Self-Consistent Structure of Metallic Hydrogen," Phys. Rev. Lett. 38, 415-418 (1977).

[57] J. K. Krause and C. A. Swenson, "Direct Measurements of the Constant-Volume Heat Capacity of Solid Parahydrogen from 22.79 to 16.19 cm3/mole and the Resulting Equation of State," Phys. Rev. B 21, 2533-2548 (1980).

[58] V. Diatschenko, C. W. Chu, D. H. Liebenberg, D. A. Young, M. Ross, and R. L. Mills, "Melting Curves of Molecular Hydrogen and Molecular Deuterium Under High Pressures," Phys. Rev. B 32, 381-389 (1985).

[59] G. I. Kerley and J. Abdallah, Jr., "Theoretical Equations of State for Molecular Fluids: Nitrogen, Oxygen, and Carbon Monoxide," J. Chem. Phys. 73, 5337-5350 (1980).

[60] G. I. Kerley, "A Theoretical Equation of State for Methane," J. Appl. Phys. 51, 5368-5374 (1980).

[61] G. Fiorese, "Monte Carlo Calculations for Molecular H_2 in the Fluid Phase," J. Chem. Phys. 73, 6308-6315 (1980). G. Fiorese, "A Theoretical Equation of State for Molecular Hydrogen," J. Chem. Phys. 75, 1427-1433 (1981).

[62] G. I. Kerley, "Theoretical Equation of State for Aluminum," Int. J. Impact Engng. 5, 441-449 (1987)

[63] G. I. Kerley, "Multiphase Equation of State for Iron," Sandia National Laboratories report SAND93-0027, 1993.

[64] G. I. Kerley, "Equations of State for Copper and Lead," Kerley Technical Services report KTS02-1, February 2002.

[65] G. I. Kerley, "Equations of State for Be, Ni, W, and Au," Sandia National Laboratories report SAND2003-3784, October 2003.

[66] G. I. Kerley, "Equations of State for Titanium and Ti6Al4V Alloy," Sandia National Laboratories report SAND2003-3785, October 2003.

[67] G. I. Kerley, "Equations of State for Calcite Materials. I. Theoretical Model for Dry Calcium Carbonate," High Press. Res. 2, 29-47 (1989).

[68] Y. Rosenfeld, "On Equation of State Calculations from Experimental Zero-Kelvin Isotherms," J. Chem. Phys. 73, 5753-5769 (1980).

[69] Y. Rosenfeld, "Equations of State for Liquids from the Zero-Kelvin Isotherm: Quantum Corrections for Hydrogen," J. Chem. Phys. 73, 5760-5765 (1980).

[70] B. P. Singh and S. K. Sinha, "Quantum Corrections to the Equilibrium Properties of Dense Fluids: Application to Hard Sphere Fluids, " J. Chem. Phys. 67, 3645-3649 (1977).

[71] R. L. Mills, D. H. Liebenberg, J. C. Bronson, and L. C. Schmidt, "Equation of State of Fluid n-H2 from P-V-T and Sound Velocity Measurements to 20 Kbar," J. Chem. Phys. 66, 3076-3084 (1977).

[72] D. H. Liebenberg, R. L. Mills, and J. C. Bronson, "Thermodynamic Properties of Fluid n-H2 in the Range 75-307 K and 2-20 kbar," Los Alamos Scientific Laboratory report LA-6645-MS (1977).

[73] R. L. Mills, D. H. Liebenberg, and J. C. Bronson, "Equation of State of Fluid n-D2 from P-V-T and Ultrasonic Velocity Measurements to 20 Kbar," J. Chem. Phys. 68, 2663-2668 (1978).

[74] D. H. Liebenberg, R. L. Mills, and J. C. Bronson, "Thermodynamic Properties of Fluid n-D2 in the 75 to 300 K and 2- to 20-kbar Range," Los Alamos Scientific Laboratory report LA-7007-MS (1978).

[75] B.-J. Yoon and H. A. Scheraga, "Monte Carlo Simulation of the Hard-Sphere Fluid with Quantum Correction and Estimate of Its Free Energy," J. Chem. Phys. 88, 3923-3933 (1988).

[76] L. M. Sese, "Thermodynamic and Structural Properties of the Path-Integral Quantum Hard-Sphere Fluid," J. Chem. Phys. 108, 9086-9097 (1998).

[77] S. B. Kormer, A. I. Funtikov, V. D. Urlin, and A. N. Kolesnikova, "Dynamic Compression of Porous Metals and the Equation of State with Variable Specific Heat at High Temperatures," Sov. Phys. JETP 15,477-488 (1962).

[78] M. W. Chase, Jr., C. A. Davies, J. R. Downey, Jr., D. J. Frurip, R. A. McDonald, and A. N. Syverud, "JANAF Thermochemical Tables," J. Phys. Chem. Ref. Data 14, Supp. No. 1 (1985).

[79] M. N. Saha, Philos. Mag. 40, 472 (1920); Proc. R. Soc. London Ser. A 99, 135 (1921).

[80] R. M. More, "Atoms in Dense Plasmas," Lawrence Livermore National Laboratory report UCRL-93926, January 1986.

[81] D. A. Liberman, "Self-Consistent Field Model for Condensed Matter," Phys. Rev. B **20**, 4981-4989 (1979).

[82] G. I. Kerley, "Atomic Orbital Data for Elements with Atomic Numbers $1 \leq Z \leq 103$," Sandia National Laboratories report SAND88-2594, 1988.

[83] G. I. Kerley, "Modification of the Lee-More Conductivity Model: Improved Calculation of Ionization State," Kerley Publishing Services report KPS99-2, Albuquerque, NM, February 1999.

[84] Thermophysical Properties of Fluid Systems, NIST Webbook, http://webbook.nist.gov/chemistry/fluid.

[85] E. M. Brody, H. Shimizu, H. K. Mao, P. M. Bell, and W. A. Bassett, "Acoustic Velocity and Refractive Index of Fluid Hydrogen and Deuterium at High Pressures," J. Appl. Phys. 52, 3583-3585 (1981).

[86] T. S. Duffy, W. Vos, C. S. Zha, R. J. Hemley, and H. K. Mao, "Sound Velocities in Dense Hydrogen and the Interior of Jupiter," Science 263, 1590-1593 (1994).

[87] N. C. Holmes, M. Ross, and W. J. Nellis, "Temperature Measurements and Dissociation of Shock-Compressed Liquid Deuterium and Hydrogen," Phys. Rev. B 52, 15835-15845 (1995).

[88] M. D. Knudson, "Absolute Hugoniot Measurements of Aluminum to ~5 Mbar Using Magnetically Driven Flyer Plates," presented at APS Conference, Division of Plasma Physics, Oct. 2001. Also personal communication.

[89] J. F. Barnes and S. Lyon, Los Alamos National Laboratory report LA-11058-MS.

[90] P. G. Klemens, "Theory of Thermal Conductivity of Dielectric Solids: Effects of Defects and Microstructure at High Temperatures," in Proceedings of the Seventh Symposium on Thermophysical Properties, edited by A. Cezairlyan (ASME, 1977) pp. 100-104.

[91] W. J. Nellis, A. C. Mitchell, P. C. McCandless, D. J. Erskine, and S. T. Weir, "Electronic Energy Gap of Molecular Hydrogen from Electrical Conductivity Measurements at High Shock Pressures," Phys. Rev. Lett. 68, 2937-2940 (1992).

[92] V. E. Fortov, V. Ya. Ternovoi, S. V. Kvitov, V. B. Mintsev, D. N. Nikolaev, A. A. Pyalling, A. S. Filimonov, "Thermodynamic Properties and Electrical Conductivity of Hydrogen at Multiple Shock Compression up to 150 GPa Pres-

sure Ionization," in Shock Compression of Condensed Matter - 1999, edited by M. D. Furnish, L. C. Chhabildas, and R. S. Hixson (AIP Conference Proceedings 505, 2000) pp. 49-52.

[93] Y. T. Lee and R. M. More, "An Electron Conductivity Model for Dense Plasmas," Phys. Fluids 27, 1273-1286 (1984).

[94] R. M. More, "Atomic Physics of Laser-Produced Plasmas," in Handbook of Plasma Physics, edited by M. N. Rosenbluth and R. Z. Sagdeev (Elsevier Science Publishers, 1991) Chapter 2, pp. 63-110.

[95] A. V. Farnsworth, Sandia National Laboratories, personal communication. The Lee-More model used in this work was taken from a Sandia code. The Sandia version reproduces subroutines obtained from Lawrence Livermore Laboratory, which included the Zimmerman electron-electron scattering correction. We have not yet found a reference to this correction.

[96] W. C. DeMarcus, "The Constitution of Jupiter and Saturn," ApJ. 63, 2-28 (1958).

[97] W. B. Hubbard and R. Smoluchowski, "Structure of Jupiter and Saturn," Space Sci. Rev. 14, 599-662 (1973).

[98] G. Chabrier, D. Saumon, W. B. Hubbard, and J. I. Lunine, "The Molecular-Metallic Transition of Hydrogen and the Structure of Jupiter and Saturn," ApJ. 391, 817-826 (1992).

[99] F. Gygi and G. Galli, "Electronic Excitations and the Compressibility of Deuterium," Phys. Rev. B 65, 220102-1,4 (2002).

[100] M. W. C. Dharma-wardana and F. Perrot, "The Equation of State and the Hugoniot of Laser Shock-Compressed Deuterium," E-Print ArXiv paper, (Dec. 2001).

Appendix A

D_2 Hugoniot Data from Laser Experiments

Throughout this report, we have ignored the deuterium Hugoniot data from the Nova laser experiments [28]-[30] in making comparisons with our EOS model. As stated in Sec. 1, we believe that the laser data either contain systematic errors or nonequilibrium effects that have not been identified. This appendix presents some calculations that support that opinion.

Figure 22 compares the Nova laser data (X's) with the gas-gun data of Nellis, et al. [4] and the Z-machine data of Knudson, et al. [6]-[8] (circles). The Nova data show a maximum compression of ~ 6.2, while the data of Knudson, et al. show a maximum shock compression of ~ 4.2. Nellis has noted that the high compressions seen in the laser data are inconsistent with data for other diatomic molecules and has discussed possible causes of error in the laser experiments [33]. *Ab initio* numerical calculations [22][23][25] also disagree with the laser data.

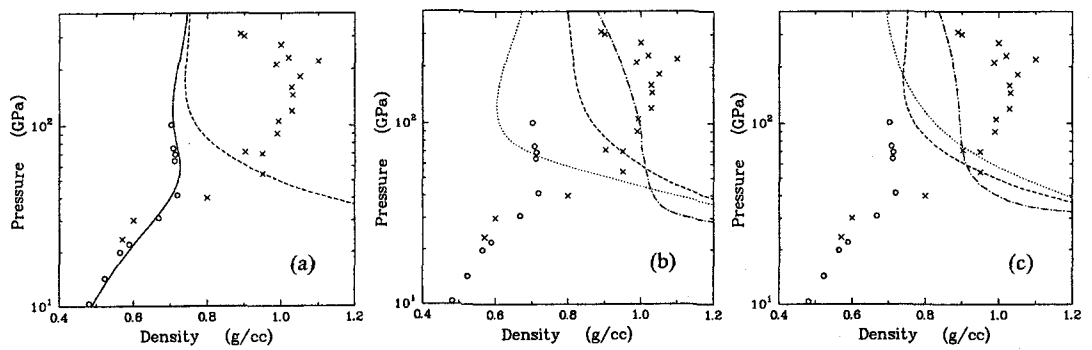

Fig. 22. Comparisons with laser Hugoniot data. Experimental data: circles [4][6]-[8], X's [28]-[30]. Model calculations (a): solid line—complete model, dashed line—*atomic fluid* only. Sensitivity tests (b): dotted line—solid-gas model, dashed line—solid with ideal gas ion motion, dotdashed line—solid with no ion motion. Sensitivity tests (c): dashed line—equilibrium fluid as in (a), dotdashed line—hot electrons, dotted line—cold electrons.

When the laser data first appeared, it was thought that the high compressions were due to dissociation. We have already shown that our model does predict the onset of dissociation at about 20 GPa on the Hugoniot but that it is inconsistent with the laser data. The solid line in Fig. 22a shows the Hugoniot calculated using the full EOS model, including both molecular and atomic species. The dashed line in Fig. 22a shows the Hugoniot calculated using only the atomic species, i.e., when dissociation is forced to occur. The calculations do not predict the high compressions seen in the laser experiments, even when dissociation is complete.

Clearly, a drastic revision of our EOS for the atomic fluid would be required to match the laser data.

Several calculations were made to examine what changes in the atomic model would improve agreement with the laser data. The results are shown in Fig. 22b. The dotted line was calculated using an EOS like that for the atomic solid (Sec. 3.1), except that the lattice vibrational terms were replaced by a formula that interpolates between the Debye model at low temperatures and an ideal gas model at high temperatures. (See Sec. 4.3 of the PANDA manual for details.) This "solid-gas" EOS gives much poorer agreement with the laser data (as well as the other data) than our more fundamental liquid perturbation model. The dashed line was computed by using the ideal gas formula at all temperatures. This ideal gas model gives higher compressions but still fails to match the laser data. In order to match the data, it is necessary to eliminate the contributions from thermal ion motion altogether, as shown by the dotdashed line. This model is not credible, of course; we include it only to demonstrate what drastic changes to the atomic fluid model are required to be consistent with the laser experiments.

It does not appear possible to match the laser data with any reasonable EOS model for the atomic fluid. This fact, together with the evidence from the other experiments and the *ab initio* calculations, is compelling evidence that the laser data do not represent an *equilibrium* material response. However, it has been proposed that *nonequilibrium* phenomena could be important on the time scale of the laser experiments.

Gygi and Galli [99] suggested that shock-induced electronic excitations could be responsible for the anomalously high shock compressions. The dotdashed line in Fig. 22c was computed using our model for the atomic fluid, but taking the electrons to be ten times hotter than the nuclei in computing the thermal electronic contributions. This "hot electron" model does indeed give higher compressions than the equilibrium model (dashed line) at high pressures, but it falls far short of matching the laser data. In addition, it is not clear what mechanism could produce such high electron temperatures.

Dharma-wardana and Perrot [100] made the opposite argument—that the ions should initially be much hotter than the electrons. The dotted line in Fig. 22c was computed using our model for the atomic fluid, but taking the electrons to be ten times colder than the nuclei. This "cold electron" model gives slightly higher compressions than the equilibrium model at the lower pressures but gives an even stiffer Hugoniot at the high pressures.

Nonequilibrium behavior cannot yet be ruled out as an explanation for the anomalously high compressions seen in the laser experiments. However, we believe that the phenomena and mechanisms involved have not yet been identified.

Appendix B

The Conductivity Model

This appendix discusses our modifications to the Lee-More-Zimmerman (LMZ) conductivity model that was used in Sec. 10.8. The basic equations are the same as those given in the 1991 article by More [94], except that they include a correction for electron-electron scattering that is attributed to G. B. Zimmerman [95]. We have modified these equations to use the ionization state and melting curves from our EOS model.

The basic LMZ equation for the electrical conductivity is

$$\sigma = 2.818 \times 10^{-4} z_F n_i \tau_e A_\mu S_\mu \ \Omega^{-1}\text{cm}^{-1}. \tag{B.1}$$

Here z_F is the ionization state (number of free electrons/atom), n_i is the ion density (number of atoms/cm^3), and τ_e is the electron relaxation time in sec. The electron chemical potential μ is defined by treating the free electrons as an ideal Fermi gas. A_μ is a function of μ that varies between 1 and 3.4. S_μ is the Zimmerman electon-electron scattering correction,

$$S_\mu = z_F f_\mu / (1 + z_F f_\mu), f_\mu = 1 + \ln[1 + \exp(\beta\mu)]. \tag{B.2}$$

(This correction is very important in the present case, where the levels of ionization are low.)

The electron relaxation time, or time between collisions, is computed using several approximations, each of which apply to different regions of density and temperature. In this work, we need be concerned only with regions 4, 5, and 6.

In Region 5, which corresponds to the highest densities and lowest temperatures, the relaxation time is given by the Bloch-Grüneisen law modified by the Lindemann approximation,

$$\tau_e = \tau_{BG} = 50(r_s/v_e)(T_m/T) \text{ (Region 5)}. \tag{B.3}$$

Here r_s is the ion-sphere radius, v_e is the average electron velocity (Eq. 3.21 of Ref. [94]), and T_m is the melting temperature, a function of density.

In Region 6, which corresponds to temperatures $T > T_m$, the relaxation time from Eq. (B.3) is modified by an approximation suitable for liquids,

$$\tau_e = \tau_{liq} = \tau_{BG}/1.35 \text{ (Region 6)}. \tag{B.4}$$

Region 4 is introduced to ensure that the mean free path is not less than the ion-sphere radius.

$$\tau_e = \tau_4 = r_s/v_e \text{ (Region 4)}, \tag{B.5}$$

which applies if $\tau_4 > \tau_{BG}$ (for $T < T_m$) or $\tau_4 > \tau_{liq}$ (for $T > T_m$).

In the standard LMZ model, the ionization state is computed from the Thomas-Fermi formula, and the melting temperature is computed from a formula due to Cowan. Neither approximation gives reasonable results for the hydrogen isotopes.

In the present work, we modified the LMZ model to use the ionization state and melting curve from our EOS model. Calculation of the ionization state is described in Sec. 9.7. Since the Bloch-Grüneisen law, Eq. (B.3), applies to metals, we used the melting temperature for the atomic solid, rather than for the molecular solid. (The conductivities would be about 4-7 times higher if we used the molecuar melting curve.)

When the ionization state and melting curve are modified, the LMZ model predicts the states obtained in the reverberation experiments to lie in Region 6. For the D_2 Hugoniot, the states lie in Region 6 for pressures up to 18 GPa and Region 4 at higher pressures.

We also made calculations in which Regions 5 and 6 were eliminated, forcing the model to use a relaxation time determined strictly by the ion sphere radius. This change had only a small effect on the conductivity on the Hugoniot. As expected, it predicted lower conductivities for the reverberation experiments, giving somewhat poorer agreement with the data. However, it still predicted the general trends, including the large difference between the Hugoniot and reverberation experiments.

The LMZ model also includes multipliers, in Eqs. (B.3) and (B.5), that could be adjusted to improve agreement with the experimental data. However, we have not used those parameters in the present work.

Distribution

1 Alliant TechSystems
Attn: Frederick Stecher
MS: MN07-MW44
4700 Nathan Lane N.
Plymouth, MN 55442-2512

3 Applied Research Associates, Inc.
Attn: Dennis Grady
Craig Doolittle
K. Bryan Milligan
4300 San Mateo Blvd. NE, Suite A-220
Albuquerque, NM 87110

1 Applied Research Associates, Inc.
Attn: William Brown
2760 Eisenhower Ave., Suite 308
Alexandria, VA 22314

1 Applied Research Associates
Attn: Peter Dzwilewski
5941 South Middlefield Rd., Suite 100
Littleton, CO 80123

2 Battelle Memorial Institute
Attn: Dale Trott
Mike Fisher
505 King Ave.
Columbus, OH 43201-2693

1 Boeing Corporation
Attn: Kevin Housen
MS 2T-50
P. O. Box 3999
Seattle, WA 98124

1 Boeing Company
Attn: Irene Aronoff
MC QB-62
PO Box 7922
Canoga Park, CA 91309-7922

1 Brown University
Attn: Peter Schultz
Dept. of Geological Sciences
P.O. Box 1846
Providence, RI 02912

1 Brigham Young University
Attn: Carl Sorenson
Dept. of Mech. Engineering
Provo, UT 84602

1 California Institute of Technology
Attn: Thomas Ahrens
Seismological Laboratory
1299 E. California Blvd.
Pasadena, CA 91125

1 California Institute of Technology
Attn: Joseph Shepherd
Engineering and Applied Science
MC 105-50
Pasadena, CA 91125

3 Carnegie Institution of Washington
Geophysical Laboratory
Attn: T. S. Duffy
R. M. Hemley
H. K. Mao
5251 Broad Branch Rd., NW
Washington, DC 20015

1 Cornell University
Department of Physics
Attn: Neil W. Ashcroft
Ithaca, NY 14853

1 Cornell University
Materials Science & Engineering
Attn: Arthur L. Ruoff
Ithaca, NY 14853

1 Enig Associates, Inc.
Attn: Julius W. Enig
11120 New Hampshire Ave., Suite 500
Silver Spring, MD 20904-26

1 Harvard University
Attn: Sarah Stewart-Mukhopadhyay
Department of Earth & Planetary Sciences
Cambridge, MA 02138

1 Institute for Defense Analyses
Attn: Bohdan Balko
1801 North Beauregard Street
Alexandria, VA 22311

15 Kerley Technical Services
Attn: Gerald I. Kerley, Consultant
P.O. Box 709
Appomattox, VA 24522-0709

1 KTech
Attn: Larry Lee
2201 Buena Vista SE, Suite 400A
Albuquerque, NM 87106-4265

2 Lockheed Martin Missiles Space Systems
Missiles & Space Operations
Attn: Erik Matheson
Luen Tam
1111 Lockheed Martin Way
Sunnyvale, CA 94089

2 NASA Johnson Space Center
Attn: Eric L. Christiansen
Justin H. Kerr
Mail Code SN3
Houston, TX 77058

2 NASA/Langley Research Center
Attn: Scott A. Hill, MS 431
Carl Poteet, MS 396
1 North Dryden St.
Hampton, VA 23681-2199

5 Naval Air Warfare Center
Attn: Joseph B. Bickley
Thomas J. Gill
John Kandell
Kelly Minnick
Edwin Szymanski
1 Administrative Circle
China Lake, CA 93555

1 Naval Postgraduate School
ELectrical & Computer Engineering Dept.
Attn: Donald Wadsworth
833 Dyer Road, Bldg. 232
Monterey, CA 93943-5121

7 Naval Surface Warfare Center
Dahlgren Division
Attn: J. R. Cogar
R. Gamache
R. K. Garrett, Jr.
M. Hobson
D. F. Robinson
D. Vavrick
L. T. Wilson
17320 Dahlgren Rd.
Dahlgren, VA 22448

6 Naval Surface Warfare Center
Indian Head Division
Attn: Bill Lawrence
Phil Miller
Thomas P. Russell
Gerrit Sutherland
Daniel Tam
Frank J. Zerilli
101 Strauss Avenue
Indian Head, MD 20640-5035

2 Network Computing Services, Inc.
AHPCRC
Attn: Gordon R. Johnson
Tim Holmquist
1200 Washington Avenue South
Minneapolis, MN 55415

1 New Mexico State Inst. of Mining & Tech.
Attn: Robert Abernathy
EMRTC Center
Socorro, NM 87801

1 Oak Ridge National Laboratory
Attn: Seokho Kim
P. O. Box 2009
Oak Ridge, TN 37831-8045

1 Plattsburgh State University
Department of Physics
Attn: Paul P. Szydlik
101 Broad Street
Plattsburg, NY 12901-2681

1 Schlumberger Reservoir Completions
Center, Perforating Gun Systems
Attn: Wenbo Yang
14910 Airline Road
Rosharon, TX 77583

1 Science Applications International Corp.
Attn: Gerry Gurtman
10260 Campus Point Drive
San Diego, CA 92121

1 Science Applications International Corp.
Attn: Mark E. Beyers
1710 SAIC Drive
McLean, VA 22102

2 Southwest Research Institute
Attn: Charles E.Anderson
James Walker
P. O. Drawer 28510
San Antonio, TX 78228-0510

1 Texas A&M University
Nuclear Engineering Dept.
Attn: Bruce L. Freeman
Zachry Building, Room 129
College Station, Texas 77843-3133

1 Texas Tech University
Department of Mechanical Engineering
Attn: Darryl James
Box 41021
Lubbock, TX 79409-1021

2 Thiokol Corporation
Science & Engineering Division
Attn: Robert L. Hatch, Mailstop 244
Dwight Clark, Mailstop 280
P. O. Box 707
Brigham City, Utah 84302-0707

1 University of Alabama in Huntsville
Aerophysics Department
Attn: Mark Zweiner
P.O. Box 999
Huntsville, AL 35899

2 University of Arizona
Department of Planetary Sciences
Attn: W. B. Hubbard
H. J. Melosh
Tucson, AZ 85721

1 University of California
Attn: Raymond Jeanloz
Earth and Planetary Science
Berkeley, CA 94720-4767

15 University of California
Lawrence Livermore National Laboratory
Attn: R. Cauble
G. W. Collins
H. C. Graboske
J. Heidrich
N. C. Holmes
B. Militzer
B. Moran
J. A. Moriarty
A. K. McMahan
W. J. Nellis
P. C. Souers
C. M. Tarver
S. T. Weir
D. A. Young
G. B. Zimmerman
P.O. Box 808
Livermore, CA 94550

18 University of California
Los Alamos National Laboratory
Attn: Chris Adams
J. Boettger
L. A. Collins
L. L. Davis
R. Gustavsen
R. S. Hixson
B. L. Holian
Y. Horie
J. D. Johnson
J. E. Kennedy
J. D. Kress
J. Mace
E. S. Martin
R. Parker
J. M. Pedicini
J. P. Ritchie
S. Sheffield
D. Saumon
P.O. Box 1663
Los Alamos, NM 87545

1 University of Illinois
Attn: David M. Ceperley
Department of Physics
1110 W. Green Street
Urbana, IL 61801

1 University of Missouri-Rolla
CE Department
Attn: William Schonberg
Rolla, MO 65409

1 University of Notre Dame
Dept. of Aerospace and Mech. Eng.
Attn: Joseph M. Powers
372 Fitzpatrick Hall of Engineering
Notre Dame, Indiana 46556-5637

1 University of Rochester
Laboratory for Laser Energetics
Attn: R. L. McCrory
250 East River Road
Rochester, NY 14623-1299

1 University of Rochester
Physics & Astronomy
Attn: Hugh M. Van Horn
RC Box 270171
Rochester, NY 14627-0171

2 The University of Texas at Austin
Institute for Advanced Technology
Attn: Stephan J. Bless
David Littlefield
4030 W. Braker Lane, Suite 200
Austin, TX 78712

1 University of Texas at El Paso
Mechanical & Industrial Engineering
Attn: Michael Huerta
500 West University Avenue
El Paso, TX 79968

1 University of Washington
Dept. of Aeronautics and Astronautics
Attn: Keith A. Holsapple, FS10
Seattle, WA 98195

1 U.S. Air Force Inst. of Technology/ENY
Attn: Jay R. Anderson
Wright-Patterson AFB, OH 45433

1 U.S. Air Force Research Laboratory
Attn: David F. Medina
3550 Aberdeen Ave SE
Kirtland AFB, NM 87117-5776

11 U.S. Army Research Laboratory
Attn: W. Bruchey
D. Dandekar
F. Gregory
A. D. Gupta
Y. Huang
K. D. Kimsey
B. Leavy
H. Meyer, Jr.
M. L. Normandia
S. Schoenfeld
J. Starkenberg
P.O. Box 334, Main Station
Aberdeen Proving Ground, MD 21005

3 U.S. Army Space & Missile Defense Command
Attn: Robert Becker
Jason McCullough
Tim Reid
PO Box 1500
Huntsville, AL 35807-3801

2 U. S. Army TACOM-ARDEC
SMCAR-AEE-WW
Attn: Ernest L. Baker
Chuck Chin
Picatinny Arsenal, NJ 07806-5000

2 Washington State University
Department of Physics
Shock Dynamics Laboratory
Attn: James R. Asay
Yogendra M. Gupta
Pullman, WA 99164-2814

2 Wright Laboratory
Attn: Dan Brubaker
William Cook
Bruce C. Patterson
Eglin AFB, FL 32542-5434

1 NIMIC, NATO Headquarters
Attn: Peter R. Lee
B-1110 Brussels
BELGIUM

1 M. W. C Dharma-wardana
National Research Council
Ottowa
CANADA K1A 0R6

1 University of British Columbia
Attn: Andrew Ng
Department of Physics & Astronomy

6224 Agricultural Road
Vancouver, BC V6T 1Z1
CANADA

1 Groupe d'Astrophysique (CNRS)
Attn: G. Chabrier
Ecole Normale Supérieure
46 Alée d'Italie
68364 Lyon Cedex 07
FRANCE

2 Commissariat à l'Energie Atomique
Centre d'Etudes de Bruyères-le-Châtel
Attn: Philippe Arnault
Dominique Gilles
BP 12, F91680 Bruyères-le-Châtel
FRANCE

1 Commissariat a l'Energie Atomique
Attn: Jean-Paul Plotard
Coutry, 77181
FRANCE

1 French German Research Institute (ISL)
Attn: Lionel Bourne
5, Rue de General Cassagnon
Saint-Louis Cedex, 68301
FRANCE

1 Institut für Physik
Humbolt-Universität zu Berlin
Attn: Dieter Beule
Invalidenstraße 110
D-10115 Berlin
GERMANY

1 Fachbereich Physik
Universität Rostock
Attn: Ronald Redmer
Universitätsplatz 3
D-18051 Rostock
GERMANY

1 Bhaba Atomic Research Center
High Pressure Physics Division
Attn: S. K. Sikka
Bombay - 400 085
INDIA

1 National Institute for Research
Attn: Toshi Sekine
Inorganic Materials, Namiki 1-1
Tsuhuba, Ibaraki 305-0044
JAPAN

1 Weizmann Institute of Science
Attn: Zeev Zinamon
Rehovot
ISRAEL

1 Yehuda Partom
Rafael, Box 2250
Haifa, 31021
ISRAEL

1 Institute of Chemical Physics
Attn: A. N. Dremin
Russian Academy of Sciences
Moscow, 142432
RUSSIA

2 Institute for High Energy Densities
Russian Academy of Sciences
Attn: V. E. Fortov
I. V. Lomonosov
Izhorskaya ul. 13/19
Moscow, 127412
RUSSIA

1 Russian Federal Nuclear Center
Attn: V. I. Tarzhanov
P.O. Box 245
Snezhinsk, Chelyabinsk 456770
RUSSIA

1 Russian Federal Nuclear Center
Attn: R. F. Trunin
Sarov, Nizhni Novgorod Region 607190
RUSSIA

1 Manfred Held
c/o Messerschmitt-Bölkow-Blohm
GmbH AG
Postfach 1340
Schrobenhausen, 8898
GERMANY

1 M. Musella
European Commission
Joint Research Centre

European Inst. for Transuranium Elements
7615 Karlsruhe
GERMANY

2 AWE
Attn: John Maw
Peter Thompson
Aldermaston, Reading
Berkshire R57 4PR
UNITED KINGDOM

1 MS 0316 J. B. Aidun, 9235
1 0318 P. Yarrington, 9230
1 0751 R. M. Brannon, 6117
1 0819 A. C. Robinson, 9231
1 0819 R. M. Summers, 9231
1 0819 T. G. Trucano, 9211
1 0819 M. K. Wong, 9231
1 0820 P. Chavez, 9232
1 0820 A. V. Farnsworth, 9232
1 0820 M. E. Kipp, 9232
1 0820 S. A. Silling, 9232
1 0820 P. A. Taylor, 9232
1 0834 A. C. Ratzel, 9110
1 0835 E. A. Boucheron, 9141
1 0836 E. S. Hertel, 9116
1 0836 D. Crawford, 9116
1 0836 R. G. Schmidt, 9116
1 0836 M. R. Baer, 9100
1 0836 M. Hobbs, 9116
1 1168 C. Deeney, 1646
1 1168 M. D. Furnish, 1647
1 1178 D. D. Bloomquist, 1630
1 1181 L. C. Chhabildas, 1647
1 1181 J. P. Davis, 1646
1 1181 C. A. Hall, 1647
1 1181 M. Knudson, 1646
1 1181 W. D. Reinhart, 1647
1 1181 T. F. Thornhill, 1647
1 1181 T. J. Vogler, 1647
1 1185 D. P. Kelly, 15417
1 1185 R. J. Dukart, 15417
1 1185 R. J. Weir, 15417
1 1186 M. P. Desjarlais, 1674
1 1186 R. J. Lawrence, 1674
1 1190 J. P. Quintenz, 1600
1 1191 Keith Matzen, 1670
1 1194 D. H. McDaniel, 1640
1 9042 J. J. Dike, 8743
1 9018 Central Technical Files, 8945-1
2 0899 Technical Library,9616